

Analytical coarse grained potential parameterization by Reinforcement Learning for anisotropic cellulose

Xu Dong^{1,*}

¹*Department of Engineering Mechanics, Zhejiang University, Hangzhou 310027, China*

Keywords: Reinforcement Learning, Boltzmann inversion, coarse grained, cellulose, anisotropy, hydrogen bonds

Abstract

Cellulose nanocrystals (CNCs) are a type of cellulose with excellent mechanical performance and other merit attributes. According to previous reports, hydrogen bonds play a pivotal role in the anisotropic structure of the CNC. Understanding the structure and mechanical behavior of CNC on a mesoscopic scale is critical for the development and manufacture of cellulose materials. However, experimental observations and atomistic simulations are not appropriate on the mesoscopic scale. In this study, we introduce an analytical coarse-grained (CG) potential following an extended bottom-up approach that is directly parameterized using Reinforcement Learning (RL). RL is a powerful tool for industrial and academic applications in various fields. Nevertheless, the potential of RL has not yet been fully exploited in the field of molecular dynamics. The RL and Boltzmann inversion methods were employed to develop a novel CG model of cellulose to represent its anisotropy and polymer stiffness. The resultant CG model is not limited to the target properties for training, and can reproduce the dynamics mechanical properties under other circumstances without additional training. This model confirms that RL can construct a CG potential that is both physically explainable and powerful. The training code is available at <https://github.com/EiPiFun/rl-cll-cg>.

Introduction

1.1 Cellulose nanocrystals

As the most abundant natural polymer resource on Earth, cellulose is widely available and eco-friendly, with numerous natural sources including wood, bamboo, algae, and bacteria[1, 2]. Renewability, low cost, biocompatibility, biodegradability, and good mechanical performance[3, 4] are the outstanding merits of cellulose, making it a promising alternative to petroleum-based materials. As a nano-form of cellulose material, cellulose nanocrystal (CNC) can achieve superior performance, such as high elastic modulus (approximately 200 GPa), low mass density (1.6 g/cm³), high specific surface area (several hundreds of m²/g), and low coefficient of thermal expansion[4]. Owing to their excellent mechanical properties and interactions with other ions and polar molecules[5], CNCs have been widely studied and employed in biomedicine[6], water treatment[7], energy storage[8], and humidity sensors[9]. Computational simulations, including ab initio simulations[10], molecular dynamics[11], and finite element method simulations[12], were performed to reveal the molecular details and kinetics of CNC. Experimental[13–15], computational[16, 17], and analytical[18, 19] approaches have been exploited to understand the mechanical properties of CNC. Hydroxyls and HBonds play pivotal roles in these behaviors[20–22].

CNCs are composed of parallel cellulose chains and their axial elastic modulus is much larger than their transverse modulus. The covalent bonds along the cellulose chains are much stronger than the van der Waals and hydrogen bonding (HBonding) interactions in the transverse section. The axial modulus and transverse modulus of CNC are approximately 100-200 GPa and 10-50 GPa, which is confirmed by experiments[4] and simulations[16, 17]. In the transverse section, the CNCs are orthotropic and exhibit three characteristic load directions: along, perpendicular to, and slanted to the HBonding planes, as shown in Figure 1. Flat residues and HBonds are the key factors in the transverse anisotropy of cellulose. Wu et al. emphasized the anisotropy of CNC, and they simulated the stretch in three orthogonal directions (along the chain, parallel, and perpendicular to the HBonding planes) at three different strain rates and found that the mechanical properties (elastic modulus and Poisson's ratio) are highly anisotropic and independent of the strain rate[17]. When a vertical load is applied, the slant CNC model undergoing frictional sliding is ductile, whereas the vertical and horizontal models are fragile. Friction is an important mechanical behavior of CNC and has been elucidated in previous studies. The friction of the nearby cellulose layers at different velocities, normal loads, and relative angles was also simulated. They found that the number of HBonds and the distances between layers were important factors in this case[23]. Zhang et al. systematically simulated and examined the impact of the loading direction, interfacial moisture, and misalignment on the CNC-CNC interface friction mechanical behavior. The density of HBonds is strongly correlated with interaction energy in their results[24]. The frictional sliding of CNC is critical to their mechanical performance when the loading direction is slanted toward the HBonding planes.

To reflect the performance of CNC on a larger length scale, many coarse-grained (CG) models have been developed with different CG levels for different purposes such as mechanical properties and molecular interactions[25]. Phenomenon such as self-assembly or cellulose nano networks require supra CG models, in which several cellulose residues are mapped into a single bead[26–28] If the mechanical properties of the CNC are considered, one cellulose residue (one residue or two nearby residues in the same chain) is usually mapped to a bead[29, 30]. The directionality of the transverse sections was neglected.

*Corresponding author, Email: donx@zuaa.zju.edu.cn

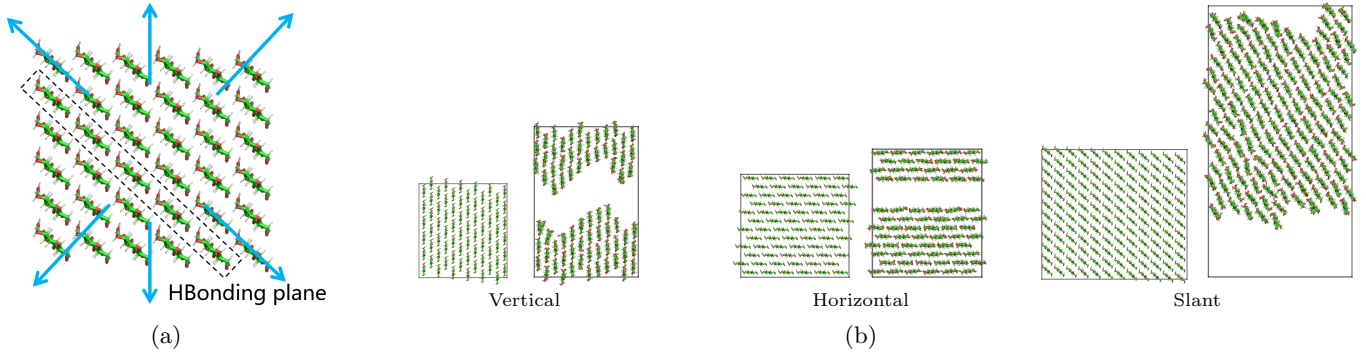


Figure 1: Orthotropic transverse section and characteristic directions. (a) Characteristic directions of orthotropic transverse sections dominated by HBonding planes. (b) Behaviors in characteristic directions. Flat residues and HBonds are critical for cellulose anisotropy. The vertical and horizontal models are dominated by HBonds and van der Waals interactions, resulting in brittle failure. The load of the slant model induced friction and rotation of cellulose residues.

Some researchers have emphasized molecular details and interactions; thus, they will preserve more molecular details and map one cellulose residue to more than one bead instead of several residues into one bead[31–34].

However, the CG models of cellulose mentioned previously could not reveal the HBond interactions and resultant directionality. Several studies have presented directionality using anisotropic particles[26, 35] or additional bonds that do not correspond to real molecular structures to compensate for the directionality [36–39]. Shishehbor et al. developed a CG CNC by matching the axial elastic modulus and transverse stress-strain curve to investigate the interface interaction and failure mechanism[38]. The CG mappings used by Shishehbor et al. neglected the flat structure of cellulose residue. Anisotropic particles and bonded (BD) directionality are unsuitable when a transverse failure mechanism with frictional sliding is considered in the CG model. Nonetheless, presenting the kinetics, energy, and mechanical properties of CG models is challenging[33].

1.2 Machine Learning parameterization and Reinforcement Learning

The data-driven Machine Learning potential may be the first consideration for a combination of Machine Learning and force fields. Machine learning models, particularly neural network models, can describe particle interactions without substantial physical or chemical intuition[40, 41]. However, significant problems remain for Machine Learning potentials, such as long-range interactions, transferability, and kinetics (particularly for CG models) are still open[40]. Neural network models also have problems with explainability[42] and computational cost. Machine learning methods can also be used to parameterize analytical force fields[43, 44]. Optimization methods, including Bayesian optimization[45], particle swarm optimization[46], genetic algorithm[47], and Gaussian process regression[48] have been used to parameterize different analytical CG potentials.

The use of Reinforcement Learning (RL) in CG simulations and potential parameterization is still in its early stages[49]. Wu et al. integrated graph attention neural networks and RL to learn CG mapping[50]. Chandra et al. used a continuous action Monte Carlo Tree Search[51] powered by RL to parameterize an analytical hybrid bond-order CG force field to simulate the aggregation of liquid-liquid mixtures[49]. RL imitates the learning of creatures and is promising for control and optimization[52, 53]. The model-free RL algorithm can deal with strongly nonlinear problems without prior expert knowledge and automatically perform trial-and-error learning procedures. More information on the RL scheme is presented in the methods section.

In summary, flat residues and HBond interactions are key features of CNC orthotropic transverse sections and their corresponding transverse mechanical behaviors, which have not been well described in previous CG models. With a tight budget for computational cost and a desire for better explainability, transferability, and kinetics, a carefully designed model with explicit analytical potential, instead of a data-driven potential model, was developed to reproduce the orthotropic mechanical behavior of the CNC. In this study, we introduce a novel CNC CG model parameterized by RL that considers flat residues, HBonds, polymer stiffness, and anisotropic mechanical performance. HBonds were implemented as nonbonded (NB) interactions with directionality in this model.

1.3 Coarse grained molecular dynamics

To better illustrate the characteristics and advantages of this CNC CG models, several classical CG modeling methods were compared as baselines in the following sections, and a brief introduction of CG modeling was necessary. CG models focus on essential features, are a compromise between accuracy/scale and computational efficiency comparing to AA models, such as the CG models of CNC on a large spatial and time scales[54]. Together with the reduction of the degrees of freedom by mapping process (replacing several atoms with a bead) and the often elimination of electrostatics interactions, the smoother and shorter energy surface from averaging over atomic structure allow them to use much longer integration timestep. Reduction + smooth energy surface + longer timestep are not only significantly fast but also beneficial for sampling collectively emergent mesoscopic behaviors or observable macroscopic properties[55]. Thereby, CG models demonstrate the

relationship between molecular scale and performances in larger scales. Although “coarse grained”, they are “fine grained” compared to continuum model and provide insights into molecular fluctuations and interactions. Well-designed CG models are especially helpful to understand the essential aspects of physical phenomena. However, the shortcomings also comes from the reduction; dynamics, non-equilibrium processes, consistence, representability, and transferability[56]. Most of the CG models concentrate on equilibrium trajectories. Pressure is an example to these problems: with much lower number of particles and velocities, even with the help of Brownian motions/Langevin dynamics, it is still hard to confirm the pressure consistence considering entropy and enthalpy, especially when transferred to a new environment. The representability problems of CG models especially for thermodynamics is the research front of many scientists[57–61].

Top-down and bottom-up are the two main paradigms for CG modeling[62]. Roughly, top-down emphasize on the emergent phenomena while bottom-up are on the basis of microscopic origins. Top-down methods are not directly connected to microscopic details, they usually utilize simple analytical functions and are hard to provide quantitative insights. Bottom-up approaches are usually structure-based, aiming at the statistical mechanics properties including many body potential of mean force, mapped probability distributions. To more accurately approximate, bottom-up usually utilize complex functions. Thus bottom-up is capable to provide quantitative description. The distinctions of there two paradigms are increasingly blurred. For instance, as a famous top-down CG potential, MARTINI also incorporate elements of bottom-up strategies[63].

MARTINI successfully reproduced the molecular structure of bilayers, hydrocarbons, and short peptides. Except for top-down MARTINI, bottom-up Iterative Boltzmann Inversion (IBI)[64], Relative Entropy (RE)[65], and Force Matching (FM)[66] were also compared as baselines. IBI is a structure-based correlation function approach to reproduce atomic radial distribution function. In IBI, all interactions are assumed as independent, thus IBI is often appropriate for ”dilute” NB pairs and ”stiff” BD interactions. RE is a variational approach to minimize the Kullback-Leibler divergence of mapped probability distribution (the configuration-dependent entropy) between AA and CG iteratively. FM is a non-iterative variational but focus on mean force of NB pairs and could be directly solved. Thereby, the FM does not guarantee to reproduce atomic distributions More descriptions and comparisons of CG modeling methods could be referred in the wonderful reviews[54–56, 62].

Although MARTINI and IBI have already been applied in the cellulose[31, 33, 67, 68], prior researches did not concentrate on the anisotropic mechanical properties, which will be further presented in the following sections. This CG model of CNC follow an extended bottom-up approach: focusing on the molecular details and mapped probability distribution. But it use simple analytical potential functions and parameterize them to reproduce mechanical properties, which is quite similar to the top-down performance-oriented philosophy. And the exploration of dynamics in CG scale is challenging. On the perspective of CG modeling, this is a hybrid-hybrid approach: hybrid both in the bottom-up/top-down approach and equilibrium/non-equilibrium contexts.

Methods

2.1 Mapping and topology

The mapping emphasizes the flat residues of the cellulose chains and the HBond interactions. One cellulose residue was mapped to one backbone CL1 bead and two branched CL2 and CL3 beads (Figure 2). Two features are considered: the distance between CL2 and CL3 in a residue and the angle of CL2-CL3 and the backbone. The first distance feature should be sufficiently long to withstand the torque and present flat residues, whereas the second angle feature should be approximately 90°. In the crystalline state, the angles of the nearby CL2:CL3-CL1(blue:orange-green) and CL3:CL2-CL1(orange:blue-green) (colons indicate that these two beads are not bonded together, whereas dash indicates bonded) are close to 180°, as illustrated in Figure 2.

Based on this mapping, we applied three types of bonds, six types of angles, and three types of improper dihedrals as the BD interactions (Figure 2). The BD interactions were designed to describe and restrain the deformations under stretching, bending, and twisting loads. To ensure restraint in the aperiodic chain (which was used for the polymer stiffness simulations during training), the CL2-CL1-CL1 and CL3-CL1-CL1 angles were categorized. A type of directional NB interaction was introduced to describe HBonds, which requires the Acceptor, Hydrogen and Donor beads. Two A:H-D topologies were determined based on the importance of HBonding and symmetries: CL2:CL3-CL1 and CL3:CL2-CL1. This directional interaction is affected by the A:H-D angle and A-D distance[69].

2.2 Potentials

In this model, the potential energy contained both BD and NB interactions.

$$V_{System} = V_{Bond} + V_{Angle} + V_{Improper} + V_{Nonbonded} \quad (1)$$

. The BD interactions were harmonic.

$$V_{Bond} = \sum k_{B,i}(r - r_{0,i})^2 \quad (2)$$

$$V_{Angle} = \sum k_{A,i}(\theta - \theta_{0,i})^2 \quad (3)$$

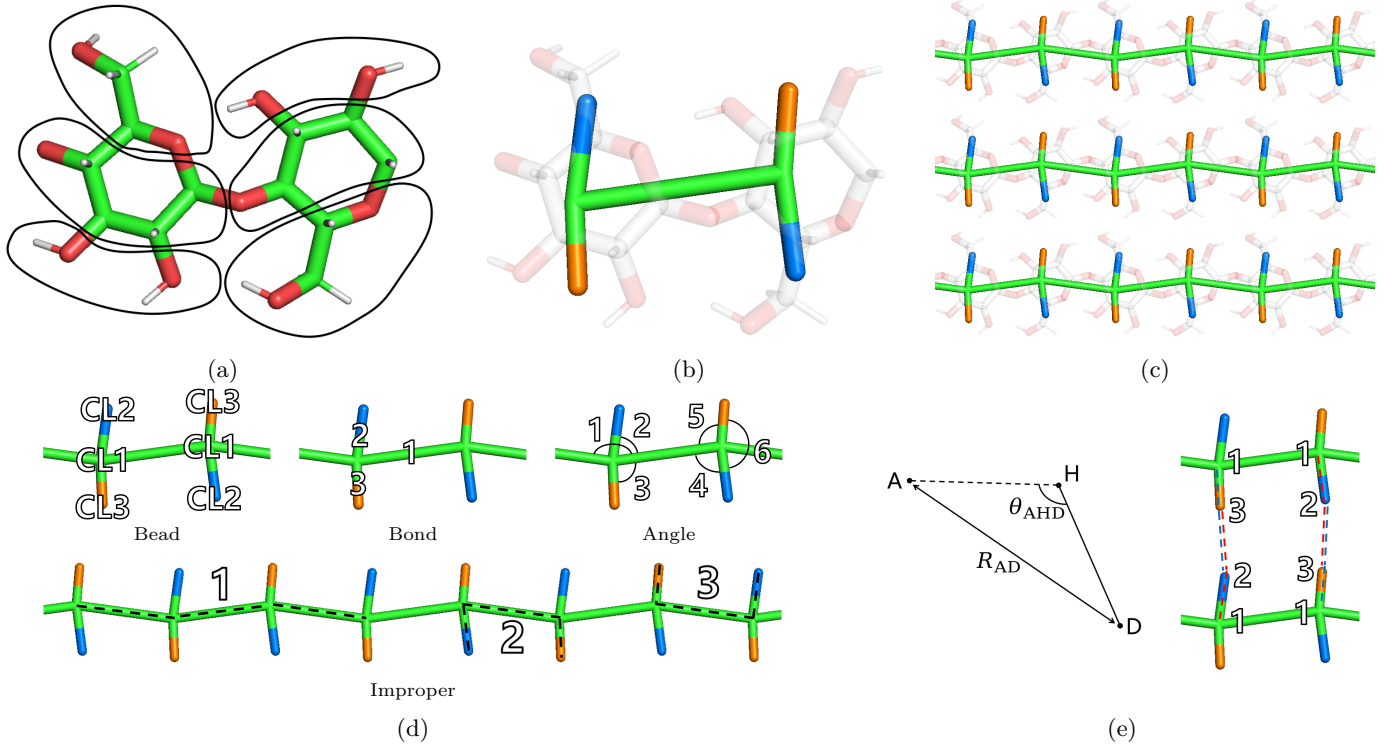


Figure 2: Mapping and topology. (a) Mapping and (b) mapped overlays for the cellulose residue and (c) laminar HBonding plane. One cellulose residue was mapped to one backbone CL1 bead and two branched CL2 and CL3 beads. The basic idea behind this mapping is to preserve the flat structure and HBonds within the HBonding layer. Qualitatively, the distance between CL2 and CL3 from the same residue was sufficient and the branched beads were expected to be perpendicular to the backbones. Under this mapping, a layer of CNC was mapped as a network structure, where the HBond interactions were stressed. (d) BD topology. BD interactions are required to preserve molecular structure and performance under stretching, bending, and twisting loads. (e) NB topology. For HBond (HB) potentials, two symmetric A:H-D relations (CL2:CL3-CL1 and CL3:CL2-CL1) were defined to describe HBonds. HB potentials were defined by using both the A:D distance and A:H-D angle.

$$V_{Improper} = \sum k_{I,i}(\chi - \chi_{0,i})^2 \quad (4)$$

. The NB interaction contained Lennard-Jones (LJ) and HBond (HB) potentials[70].

$$V_{Nonbonded} = \sum V_{LJ,i} + \sum V_{HB,i} \quad (5)$$

in which V_{LJ} and V_{HB} were in the forms

$$V_{LJ} = \begin{cases} \epsilon_{LJ} [4(\frac{\sigma_{LJ}}{r})^{12} - 4(\frac{\sigma_{LJ}}{r})^6] + V_{shift} & , 0 < r \leq r_{in} \\ \int_{r_{in}}^r [C_3(x - r_{in})^3 + C_2(x - r_{in})^2 + C_1(x - r_{in}) + C_0] dx + V_0 & , r_{in} < r \leq r_c \end{cases} \quad (6)$$

$$V_{HB} = \begin{cases} \epsilon_{HB} [5(\frac{\sigma_{HB}}{r})^{12} - 6(\frac{\sigma_{HB}}{r})^{10}] \cos^n(\theta - \theta_0 + \pi) & , 0 < r \leq r_{in} \ \& \ \theta - \theta_0 + \pi \geq \theta_c \\ S(i) \cdot \epsilon_{HB} [5(\frac{\sigma_{HB}}{r})^{12} - 6(\frac{\sigma_{HB}}{r})^{10}] \cos^n(\theta - \theta_0 + \pi) & , r_{in} < r \leq r_c \ \& \ \theta - \theta_0 + \pi \geq \theta_c \end{cases} \quad (7)$$

where:

$$S(i) = \frac{(r_c^2 - r^2)^2 [r_c^2 + 2r^2 - 3r_{in}^2]}{(r_c^2 - r_{in}^2)^3} \quad (8)$$

The LJ potential is a 12-6 formula of Lennard-Jones interactions, and the HB potential is a 12-10 formula with scaling by the power of the cosine of the A:H-D angle. Technically, these are LAMMPS[69] pair styles. The LJ potential is the lj/smooth with a shift, whereas the HB potential is a modified version of the hbond/dreiding/lj with a shift. lj/smooth is designed to smooth force to zero at the cutoff radius using a polylinear expression; this modified version of hbond/dreiding/lj ensures that potential energy reach minima at θ_0 instead of π . It should be emphasized that smoothing part between r_{in} and r_{cut} ensure the continuity of both force and energy. The energy and force curves of the HB and LJ potentials are illustrated in Figure S1.

The equilibrium A:H-D angles in the CG mapping were designed to be close to π . Even though we generalize the HB potential by adding an equilibrium angle of A:H-D, an equilibrium angle close to π is suggested to stabilize the conical energy surface.

The reason we use Lennard-Jones in th CG level was only for simplicity and the easiness to stabilize structure due to the single stationary point. The fourth power of cosine in the HB potential was the same as origin paper which proposed this formula first. For the artifacts (cut, smoothing, and directional HB potential), the sensitivity and ablation checks

were performed based on trained coefficients represented in the following sections: Half/double energy coefficients (while distance coefficients were kept), 0.8/1.2 times distance coefficients (while energy coefficients were kept), different n power of cosine, and removal of HB potential (Table S1, Table S2). These sensitivity and ablation tests confirmed the effectiveness of potentials.

2.3 Boltzmann inversion for harmonic potential

Boltzmann inversion is structure-based and is widely utilized to determine bonded potentials. Boltzmann inversion can also be integrated with Machine Learning methods to construct potentials[46, 71] or used as a baseline[72, 73].

For a harmonic potential following the Boltzmann distribution, where the bond length (or angle, or dihedral) is a deviated x around the equilibrium length x_0 :

$$\rho(x + x_0) \propto e^{-\frac{V}{k_B T}} = e^{-\frac{V_x - V_0}{k_B T}} = e^{-\frac{kx^2}{2k_B T}} \quad (9)$$

. Mark $\rho(x_0) = \rho_0$:

$$\begin{aligned} \ln \rho(x + x_0) &= -\frac{kx^2}{2k_B T} + \ln \rho_0 \\ k &= -2k_B T \cdot \frac{d[\ln \rho(x + x_0)]}{d[x^2]} \end{aligned} \quad (10)$$

. We then mark $\frac{d[\ln \rho(x + x_0)]}{d[x^2]} = \kappa$:

$$k = -2k_B T \cdot \kappa \quad (11)$$

However, the k derived must be reparameterized to represent the mechanical performance[49, 74, 75] of the CG models with fewer degrees of freedom. The effective k is k_0 times of κ :

$$k_i = k_0 \kappa_i \quad (12)$$

. Based on κ values, three k values were used for the bond, angle, and improper force constants. Considering the axial elastic modulus and polymer stiffness, k_{B0} , k_{A0} , and k_{I0} were determined via RL optimization.

2.4 Reinforcement Learning and degenerate RL

In RL, the entire problem is called the environment and the optimization program is called the agent. The environment provides at least three types of information: observation, action space, and reward. In an interaction episode with the environment, the agent selects an action a_t in the action space based on the obtained partial observation o_t of the state of the environment. The action of the agent impacts the environment evolution and is evaluated using the reward r_t function. By continuously interacting with the environment, the agent gradually learns to perform actions corresponding to a given observation to maximize the cumulative reward. The cumulative reward is defined as

$$R(\tau) = \sum_{t=0}^{\infty} \gamma^t r_t \quad (13)$$

with $\gamma \in (0, 1)$. The discount factor $\gamma \in (0, 1)$ emphasizes the latest episode and ensures numerical convergence.

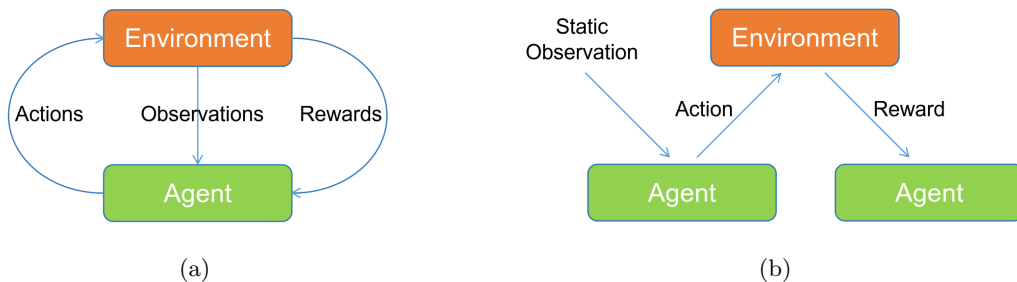


Figure 3: RL diagrams. (a) Standard RL diagram. In the standard RL diagram, the agent interacts with the environment continuously and performs actions corresponding to observations. Its optimization target is to maximize the cumulative reward $R(\tau) = \sum_{t=0}^{\infty} \gamma^t r_t$. (b) One-shot RL diagram. However, a one-shot diagram was applied and only one episode was processed. In this study, RL was employed as a nonlinear optimizer, guided by its reward function.

In this study, a degenerate version of RL was leveraged in a one-shot diagram (Figure 3). There is only one step in a learning episode, and only one reward is sampled, because the performance of a set of coefficients is independent of that of the others. Therefore, the reward can be simplified as

$$R(\tau) = r_0 \quad (14)$$

. Consequently, the RL algorithm was exploited as a nonlinear optimizer, guided under indirect supervision by a reward function. The use of degenerate RL was inspired by the work of Viquerat et al.[76], which is rare, particularly for potential parameterizations.

In this study, the RL agent was implemented using the Soft Actor Critic (SAC) algorithm[77]. SAC is the state-of-the-art algorithm recommended for continuous action space by the doc of OpenAI Stable-Baselines3[78]. The key feature is the reconciliation between the expected reward and entropy, which implies that stochasticity is included in the SAC policy to a certain extent. SAC is a gradient-free and model-free method that does not rely on a specific problem environment, and can address strongly nonlinear problems after sufficient training. Detailed information on the SAC algorithm can be obtained in the doc of OpenAI Stable-Baselines3[78].

During training, the action consists of 17 normalized coefficients ranging from [-1,1] because most RL algorithms rely on standard normal distributions[78]. The actions are linearly transformed to a physical space, which corresponds to 3 BD k , 1 HB ϵ , 1 HB σ , 6 LJ ϵ and 6 LJ σ . The reward function is a critical factor that guides the learning of the agent, and is defined by a series of matching degrees. The matching degree m for a specific performance is defined as

$$m = \frac{1}{1 + \left| \frac{y_1 - y_0}{y_0} \right|} \quad (15)$$

with a threshold m_t

$$M = \begin{cases} m & , m \geq m_t \\ 0 & , m < m_t \end{cases} \quad (16)$$

. where y_0 and y_1 are the reference and sampled values, respectively. The reward function R is the sum of a series of matching degrees, except for the transverse strength M_s and toughness M_t ,

$$R = \sum M_i + w \cdot \min(M_s, M_t) \quad (17)$$

because transverse strength and toughness were the hardest to match during the training procedures. In RL, the reward functions must be accurate and sufficiently discriminant[79]. The weights of M_s/M_t and the thresholds were designed to enhance discrimination.

2.5 Simulation setup

For both all atom (AA) and coarse-grained (CG) simulations, three models in different arrangement directions under the NPT ensemble at 0.1 MPa with a stretch load in the vertical direction were simulated. All reference AA simulations were performed using GROMACS[80, 81] and CHARMM36[82, 83] force fields (force field files were generated using CHARMM-GUI tools[84, 85]). All the CG simulations were performed using LAMMPS[69] with a self-defined force field. Referring to the performance-size curves obtained by Sinko et al.[86], we used a CNC model comprising 144 cellulose chains. Fragile vertical and horizontal models with 72 cellulose chains were used to reduce the computational cost of the simulations during training. Vertical stretches were implemented using cell deformation loads at a constant speed 10.0 nm/ns. 100 replica AA simulations with different stretch speed ranging from 0.1 nm/ns to 40.0 nm/ns were performed. The AA simulation results confirmed that the sampled strength and toughness were stable within this speed range (with deviations of less than 15%, as shown in Figure S3). Figure S4 shows the stress-strain curves of the 100 replica simulations at 10.0 nm/ns. The timestep used in the CG simulations was 4 fs for the BD properties and 12 fs for the NB properties (transverse stretching), chosen as a result of bisect between 10 fs and 15 fs. The validation for the CG timestep was provided by a 12 ns CNC equilibrium thermodynamics under NPT ensemble using 12 fs timestep S6.

2.6 Training procedures and statistics-guided reduction

Before training, the equilibrium geometry parameters (bond length l^e , angle size θ^e , and dihedral size χ^e) were derived from the mapped AA trajectories. The estimated force constants for the bonded harmonic interactions were determined using the same trajectories and Boltzmann inversion method. Three rescale factors were required for the bonds, angles, and improper dihedrals in this model. Although rescaled, the relative ratios of the force constants were maintained (e.g., the force constants for improper dihedrals were rescaled with the same factor). As previously mentioned, there are 17 coefficients, where three are BD coefficients and 14 are NB coefficients. To simplify the problem and reduce computational cost, three training stages were designed (Figure 4). The first stage was BD training for three BD k only, ignoring all NB interactions and targeting the BD properties (axial elastic modulus and polymer stiffness). We cannot determine the influence of NB interactions in the first stage, and we assume that they are not critical for the BD properties. The second stage was NB training for 14 NB coefficients with the BD coefficients obtained from the first stage, targeting the BD and NB properties (transverse strength and toughness in the three characteristic directions). The third stage was preserved only if the performance in the second stage was unsatisfactory. All properties were targeted to parameterize 17 coefficients at every turn.

The training results indicated that NB interactions did not play a pivotal role in the target BD properties. Therefore, our training ended in the second stage.

However, there was also important artificial intervention during the training process. The transverse stretch performance was sampled only once to control the cost, which was insufficient to ensure accuracy of the distribution levels between the AA

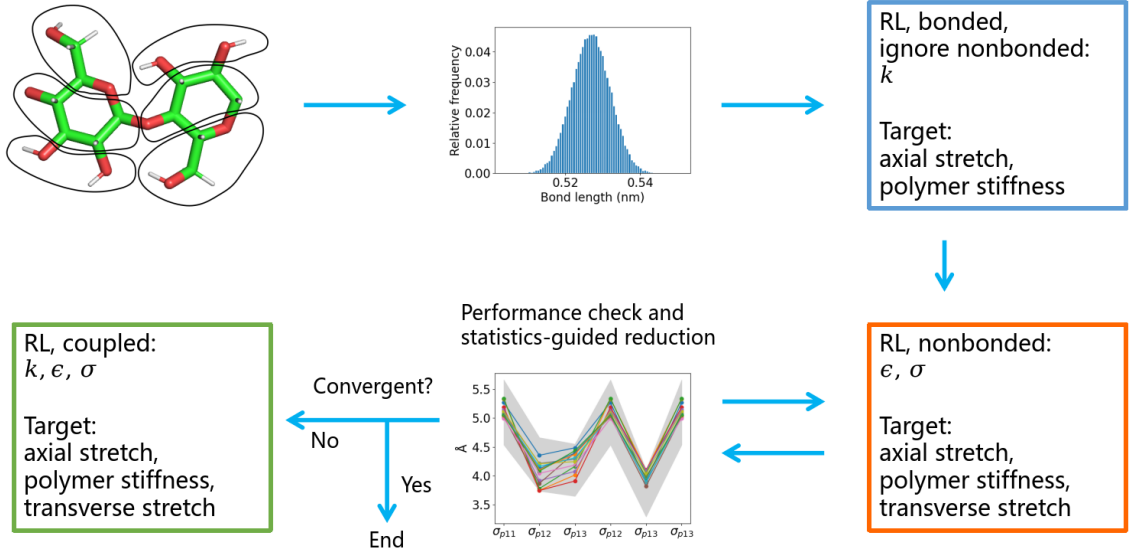


Figure 4: Training procedures. The BD properties (axial elastic modulus and polymer stiffness) and NB properties (transverse strength and toughness in characteristic directions) were the target attributes. Before training, the equilibrium bonded geometry parameters and force constants of the BD harmonic potentials were estimated from the mapped AA trajectories using the Boltzmann inversion method. In the first stage, the force constants were scaled by the RL agent in the BD training to reproduce the BD properties. In BD training, all NB interactions were ignored because we assumed that the NB interactions were not significant in this case. Given both BD and NB properties, NB training using the previously obtained BD coefficients was performed to match both BD and NB properties. However, only one batch of simulations was performed for the target properties during training. Thus, the transverse stretch performance data were manually verified through replica simulations to confirm the statistical agreement. Multiple sets of coefficients were collected to reduce the number of independent coefficients for the computational cost and physical explainability. These results confirm that our assumption of the BD properties is reasonable. Therefore, the coupled training was unnecessary.

and CG models. Therefore, manual tests for the optimized coefficients were required to verify the performance distribution, and the optimized coefficients were analyzed, inspired by Befort et al.[44]. Only coefficients with significant tendencies rather than those without clear expectations were retained as independent coefficients. These statistics-guided reduction procedures are described in the results section.

Results

3.1 Coefficients

The distance coefficients (σ) of the NB interactions were estimated using the equilibrium distance of the mapped AA trajectories. The equilibrium distance d^e is defined as the average of the minimum distances for the NB bead pairs.

$$d^e = \langle d_t^e \rangle = \langle \langle d_{tm}^e \rangle \rangle = \langle \langle \min(d_{tmn}^e) \rangle \rangle \quad (18)$$

. For the No. m CL1 bead at time t , there are n CL1 beads that are not connected to it by bonds, and the minimum distance $d_{tm}^e = \min(d_{tmn}^e)$ is sampled for this bead. For this frame, the mean $d_t^e = \langle d_{tm}^e \rangle$ of all the minimum nonbonded distances is determined for time ts . The average equilibrium distance in all trajectories $d^e = \langle d_t^e \rangle$ was defined as the equilibrium distance. As AA and CG simulation were performed under the NPT ensemble at 0.1 MPa thereby the estimation of NB σ was ranged in $[0.89d^e, 1.00d^e]$, which contains the stationary point of the LJ potential $2^{-\frac{1}{6}}$. This range was extended to $[0.89d^e, 1.11d^e]$ for the action space.

The coefficients were trained using several training loops, each containing 1024 training steps. When a training loop was completed, the information of the agent was saved and loaded for subsequent training. Considering the time consumption, 4 minutes for one trial and 3 days for a training loop was spent. The convergence criteria was defined as relative error between max reward of the latest episode and previous episodes. For the n -th training loop, the convergence criteria C was defined as the relative advantages between max reward R_n^{max} of this training loop and all of the former max reward $R_{1:n-1}^{max}$:

$$C_n = \frac{R_n^{max}}{R_{1:n-1}^{max}} \quad (19)$$

. If C_n is lower than 0.05 for 5 training loops, the training is considered as convergent. Referring to the first training loop, the last training loop achieved a higher reward much faster and more stably (Figure 5a). The average and maximum rewards of the different training loops were compared (Figure 5b) to demonstrate the convergence of training. The component match degrees of reward function with learning steps were further provided in Figure S7.

When the training was confirmed to be convergent, the coefficients with the highest reward in each training loop were extracted to determine important coefficients. The first reduction in the NB coefficients was inspired by the laminar geometry.

$$\sigma_{p11} = \sigma_{p22} = \sigma_{p33} \quad (20)$$

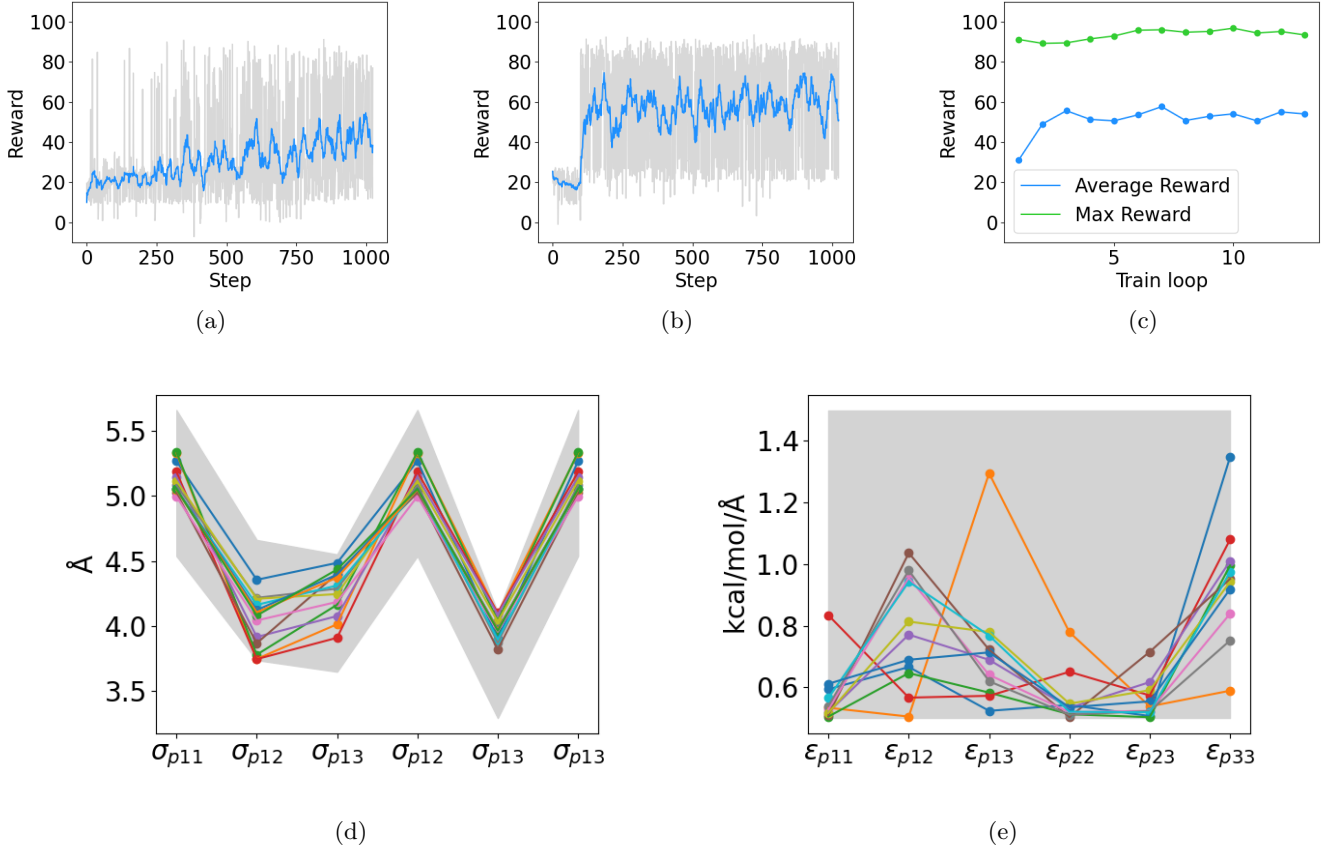


Figure 5: Training convergence and statistics-guided reduction. (a) Reward and its moving average in the first and (b) last training loops. Each training loop contained 1024 training steps. One trial took about 4 minutes and overall training took about 40 days. The subsequent training loops with higher and more stable rewards were based on the former training loops. (c) Average and maximum rewards for different training loops. The average and maximum rewards confirmed the convergence. After training, the best coefficients for the different training loops were collected to perform statistics-guided reduction. The first reduction was inferred from the geometric characteristics of the CG models, and a constraint of $\sigma_{p11} = \sigma_{p22} = \sigma_{p33}$ was applied (pmn represents a pair of CLm and CLn), which is also helpful for fragile behaviors in the vertical and horizontal directions. (d) The second reduction was in the distance coefficients using statistics. σ except for σ_{p23} oscillated around its equilibrium distance d^e whereas an obvious increase of σ_{p23} was observed. Then only σ_{p11} and σ_{p23} are kept as independent distance coefficients: $\sigma_{p12} = \frac{d^e_{p12}}{d^e_{p11}} \sigma_{p11}$, $\sigma_{p13} = \frac{d^e_{p13}}{d^e_{p11}} \sigma_{p11}$. (e) The third reduction in energy coefficients was statistically determined. After the first and second reduction, we observe that ϵ_{p23} is usually the smallest energy coefficients, which may correspond to the σ_{p23} enlargement. Then only ϵ_{p23} and ϵ_{p23} are kept as independent energy coefficient: $\epsilon_{p11} = \epsilon_{p22} = \epsilon_{p33} = \epsilon_{p12} = \epsilon_{p13}$.

where pmn is the pair of the CLm and CLn. The structures of the CG models with lower degrees of freedom were more orderly. Thus, the equilibrium distances of the same types should be nearly identical in order to represent the laminar structure. In other words, the equilibrium distance of CL1-CL1, CL2-CL2 and CL3-CL3 ought to be nearly the same, whereas in the mapped AA trajectories, they are not (Figure S12, Figure S13). The *equilibrium distances* of the ideal crystal structure were selected as the estimated value of the distance coefficient (σ) for each pair. These *equilibrium distances* do not correspond to the well-relaxed structures or characteristic distances of the radial distribution function. The first physics-informed restraint was also beneficial for reproducing fragile fractures in vertical and horizontal models.

The subsequent reductions in the NB coefficients were statistically guided.

Second reduction: Referring to d^e , only σ_{p23} had an unexpected intention to increase, maintaining σ_{p11} and σ_{p23} only.

$$\sigma_{p12} = \frac{d_{p12}^e}{d_{p11}^e} \sigma_{p11}, \sigma_{p23} = \frac{d_{p23}^e}{d_{p11}^e} \sigma_{p11}, \sigma_{p13} = \frac{d_{p13}^e}{d_{p11}^e} \sigma_{p11} \quad (21)$$

Third reduction: ϵ_{p23} were usually the smallest energy coefficients in the system, trying to keep only ϵ_{p11} and ϵ_{p23} independent

$$\epsilon_{p11} = \epsilon_{p22} = \epsilon_{p33} = \epsilon_{p12} = \epsilon_{p13} \quad (22)$$

After these dimensionality reduction, only 9 independent coefficients are preserved: 3 BD k , 1 HB ϵ , 1 HB σ , 2 LJ ϵ and 2 LJ σ .

The determined BD coefficients are listed in Table 1 and the NB coefficients are listed in Table 2. All coefficients are given with four significant digits.

These reductions and resultant coefficients informed us one thing: the sampled average values from AA trajectories could not be directly used as equilibrium points for CG interactions. The laminar structure and coefficients of CNC is critical to be artificial, and the θ_0 was also chosen of the "equilibrium angle" in the artificial model (the strict laminar model build by coordinate offset). This estimated θ_0 is beneficial but not strongly supported by molecular details.

Table 1: Bonded coefficients

type	id	$k(\text{kcal/mol}/\text{\AA}^2)$	$l_0(\text{\AA})$	$l_{AA,E}^e(\text{\AA})$	$l_{CG,E}^e(\text{\AA})$	$l_{AA,S}^e(\text{\AA})$	$l_{CG,S}^e(\text{\AA})$
bond	1	64.06	5.270	5.270	5.258	5.262	5.263
	2	82.42	2.493	2.493	2.473	2.493	2.479
	3	112.3	2.066	2.066	2.061	2.066	2.065
		$k(\text{kcal/mol})$	$\theta_0(^{\circ})$	$\theta_{AA,E}^e(^{\circ})$	$\theta_{CG,E}^e(^{\circ})$	$\theta_{AA,S}^e(^{\circ})$	$\theta_{CG,S}^e(^{\circ})$
angle	1	30.97	163.5	163.5	162.3	163.7	161.7
	2	38.79	74.2	74.2	74.7	74.2	75.4
	3	30.52	93.2	93.2	94.0	93.3	93.4
	4	27.28	90.0	90.0	89.2	90.2	89.9
	5	25.97	102.0	102.0	101.4	102.0	100.1
	6	22.42	166.3	166.3	165.1	166.5	165.1
		$k(\text{kcal/mol})$	$\chi_0(^{\circ})$	$\chi_{AA,E}^e(^{\circ})$	$\chi_{CG,E}^e(^{\circ})$	$\chi_{AA,S}^e(^{\circ})$	$\chi_{CG,S}^e(^{\circ})$
improper	1	0.1702	178.0	178.0	175.6	177.0	171.2
	2	0.1555	2.3	2.3	2.1	3.2	3.5
	3	0.1698	2.9	2.9	2.1	3.6	3.8

Table 2: Nonbonded coefficients

type	pair	$\epsilon(\text{kcal/mol})$	$\sigma(\text{\AA})$	$d_{AA,E}^e(\text{\AA})$	$d_{CG,E}^e(\text{\AA})$	$d_{AA,S}^e(\text{\AA})$	$d_{CG,S}^e(\text{\AA})$
HB	2:3-1	1.404	6.017				
	3:2-1	1.404	6.017				
LJ	1-1	0.9031	5.101	5.398	5.750	5.558	5.706
	1-2	0.9031	4.201	4.769	4.473	4.840	4.584
	1-3	0.9031	4.101	4.712	4.609	4.723	4.681
	2-2	0.9031	5.101	4.636	5.260	4.544	5.347
	2-3	0.5031	4.083	3.983	4.018	4.113	4.091
	3-3	0.9031	5.101	4.528	5.271	4.488	5.356

3.2 Bonded properties

For the BD interactions and validation of the BD coefficients, we considered the axial elastic modulus and polymer stiffness of a single cellulose chain, as listed in Table 3 and shown in Figure 6. All the values after \pm are the corresponding

standard error. Axial stretching was performed in an xyz-periodic cell with a deformation load along the chains, which is a basic mechanical property. The simulation of polymer stiffness is a single chain centered in a cell. For axial stretch, Poisson effect was presented in CG model and elastic modulus of AA and CG are 133.5 GPa and 130.3 GPa respectively, where reference modulus is 120-140 GPa[13, 14] from experiments and 110-200 GPa[16, 17, 38] from simulations. For polymer stiffness, persistence length of AA and CG range from 9.7-9.8 nm and 8.9-10.2 nm with reference data of 6-25 nm from experiments[87] and simulation[88]. Notably, the polymer stiffness data were not stable for the AA simulations because of the intertwining in some cases. Therefore, persistence lengths and end-to-end distances of different lengths (10, 20, and 30 residues) are listed. When considering polymer stiffness, the joint O atoms between two cellulose residues in the AA models and CL1 beads on the backbone in the CG models were node particles to be considered. The reference data for training were based on AA information only, and the mapped AA trajectories were compared with the CG trajectories after training. In this study, all effective k values were smaller than their estimations based on distributions (Table S3), particularly for angles and dihedrals, to reproduce the polymer stiffness performance in a system with fewer degrees of freedom (Table S4).

Table 3: Bonded properties

type		AA	CG	Error
Axial modulus (GPa)		133.5	130.5	2.25%
Persistence length (nm)	10	9.755	8.990	7.84%
	20	9.815	10.176	3.68%
	30	9.716	10.106	4.01%
End-to-end distance (nm)	10	4.523	4.529	0.01%
	20	9.355	9.199	1.67%
	30	13.536	13.432	0.77%

Table 4: Nonbonded properties

type		AA	CG	Error
Strength (MPa)	V	1224.0±9.7	1191.9±6.0	2.62%
	H	638.2±4.8	653.5±1.1	2.40%
	S	467.0±3.7	509.8±4.6	8.99%
Toughness (MPa)	V	111.0±2.5	117.0±3.2	0.54%
	H	77.9±2.8	78.1±1.2	0.26%
	S	190.1±4.6	166.9±3.8	12.20%
Direction angle	R	2.29±0.00	2.33±0.00	1.75%
	F	1.92±0.02	2.02±0.01	5.21%

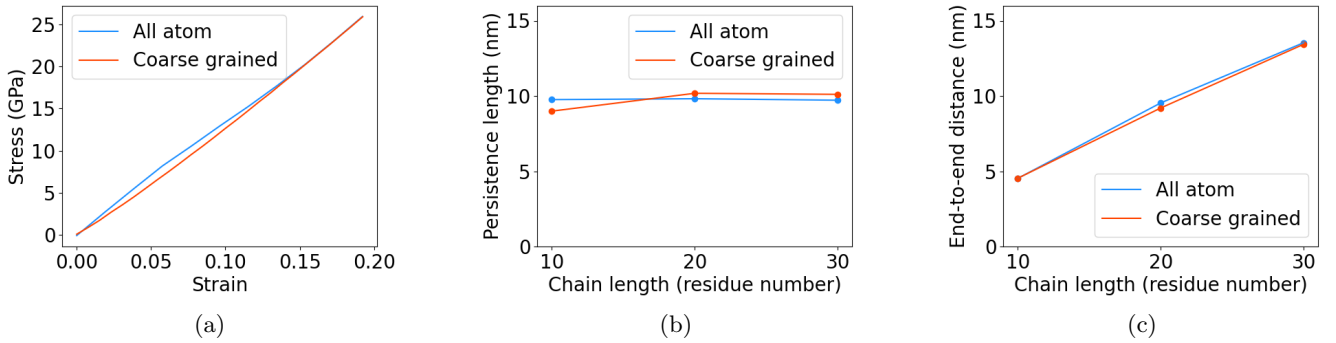


Figure 6: Bonded properties. (a) Axial elastic modulus. The elastic modulus of AA and CG are 133.5 GPa and 130.5 GPa separately, corresponding with each other and reference[38]. (b) Polymer stiffness data containing persistence length and (c) end-to-end distance. The persistence lengths of the AA and CG models with three different lengths were approximately 10 nm with errors of less than 15% and in agreement with a previous study[87]. The end-to-end distances of the AA and CG models were also similar, with errors of less than 5%.

3.3 Nonbonded properties

The NB properties include the transverse strength and toughness, as listed in Table 4. The transverse behavior of CG models are shown in Figure 7. The reference strengths of the vertical, horizontal and slant models are 0.9 GPa[17], 0.5 GPa[17] and 0.7 GPa[38], which were well reproduced by both AA and CG simulations. To reduce the effect of randomness, 100 replica simulations of transverse stretch were performed. The strength and toughness distributions of the CG models were similar to those of the AA reference data. Only the distributions of the horizontal CG models were narrower than those of their AA counterparts were. The average strength and toughness values were similar to those obtained from the AA

data. The frictional sliding of the slant models was quantitatively validated by using the direction angle (Figure S5). These data validate the CG model for reproducing the transverse anisotropy. Although all σ values were larger than expected, the equilibrium distances in the CG models were only slightly larger than those in the AA models (less than 15%, Table 2). Although the accuracy of strength and toughness distributions is problematic owing to the representability problem of CG models, the full distributions of transverse strength and toughness are shown in Figure S8 for reference. Other stretch curves collections are illustrated in Figure S9.

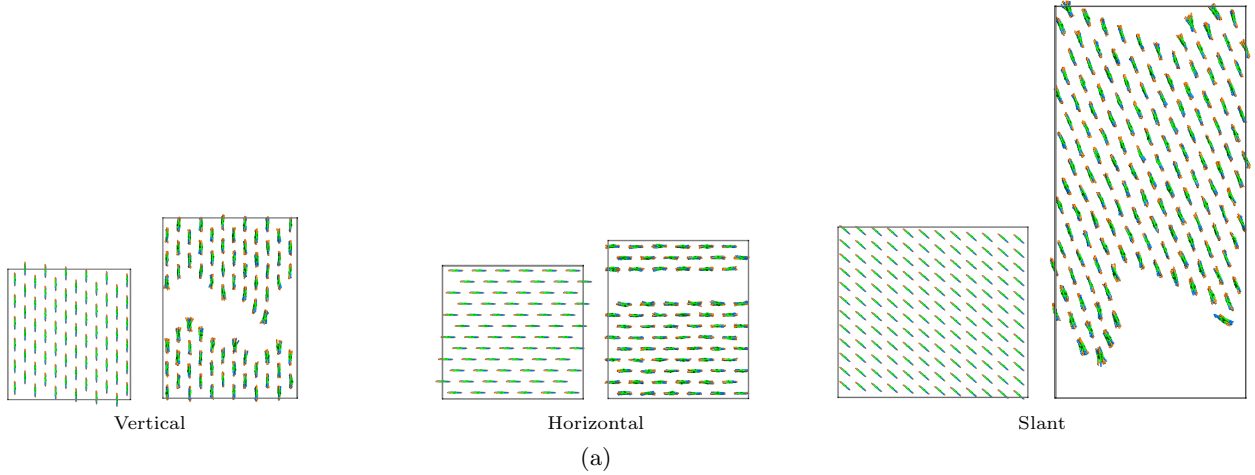


Figure 7: Transverse behaviors of CG models in the characteristic directions. Important frictional sliding in the slant direction and fragile fractures in the vertical and horizontal directions are reproduced.

3.4 Structural properties

Structural properties including BD geometry parameter distributions, NB equilibrium distance distributions, and spatial correlations are felicitous quantitative measures to validate CG models. The bond and pair distribution between CL1 and CL1, and the radical distribution function (RDF) of the whole laminar CNC, within one HBonding layer, and inter HBonding layers are shown in Figure. The RDF of one layer and inter layer were computed from sliced equilibrium structures. The alignments for the spatial correlations confirm the effectiveness of this CG model. Full comparison of the BD geometry parameter distributions and NB equilibrium distance distributions in equilibrium state and stretching progress are illustrated in Figure S10, Figure S11, Figure S12, and Figure S13. Besides, radius of gyration (R_g), and root-mean-square deviation (RMSD) of AA and CG were shown in Figure S14.

3.5 Baseline methods for coarse grained models

Except for the RL parameterized CG potential, baselines models were also tested in parallel. The simulations we used for AA and CG baselines were the slant model equilibrium without any external loads under NPT ensemble as we used for the RL parameterized model. The reference AA trajectory was simulated for 20 ns with timestep 2 fs.

Bottom-up baselines included IBI, RE, and FM and Top-down baseline MARTINI 3 were compared to illustrate the necessity of this hybrid-hybrid model. Bottom-up methods were utilized by the implementations by VOTCA[75, 89, 90]. RE is focused on NB interactions, and the BD interactions coefficients for the model were from IBI. IBI and FM models were fully independently trained 100 steps with timestep 1 fs. One trial of IBI or FM took about 8 minutes, and the 100 steps took 15 hours and 24 hours. Top-down baseline was MARTINI 3 cellulose potentials from Polyly reference[67, 91].

We felt sorry that FM to match mean forces did not produce a stable structure (it "explored" in the energy minimization). The IBI and RE models were checked under NVT ensemble without velocity generalization because the velocity and pressure manipulation would also lead to unstable structures (the periodic chains rotated and translated). Thus polymer stiffness simulation results were provided but problematic because we were not sure about the effect of velocity generalization in these cases. The transverse stretch strength and toughness were also problematic without pressure control. MARTINI 3 cellulose potentials were more robust than the bottom-up baselines and simulated under NPT ensemble.

The comparison focused on axial elastic modulus and transverse mechanical properties, as listed in Table 5 and Table 6. The worse performances of bottom-up baselines were within expectations and aligned with their limitations described in the Introduction section. It should be emphasized that all the polymer stiffness data were all from simulations with velocity generalization under NVT ensemble, regardless of the NVT or NPT marks. Except for the numerical properties in the tables, structures after relaxation and fracture are illustrated in the Figure S15 and Figure S16. Owing to its weak NB interactions and high fracture strain and toughness, fracture structures shown for MARTINI in the horizontal and slant characteristic directions was not fractured yet because it WAS stripped like a ribbon before fracture. The resultant results of these bottom-up baselines confirm the validation and superiority of this RL parameterized model following extended bottom-up approach.

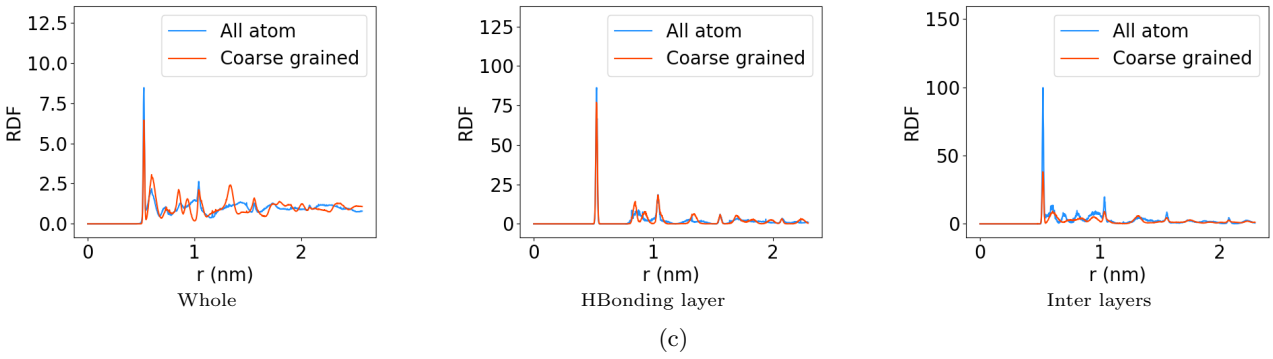
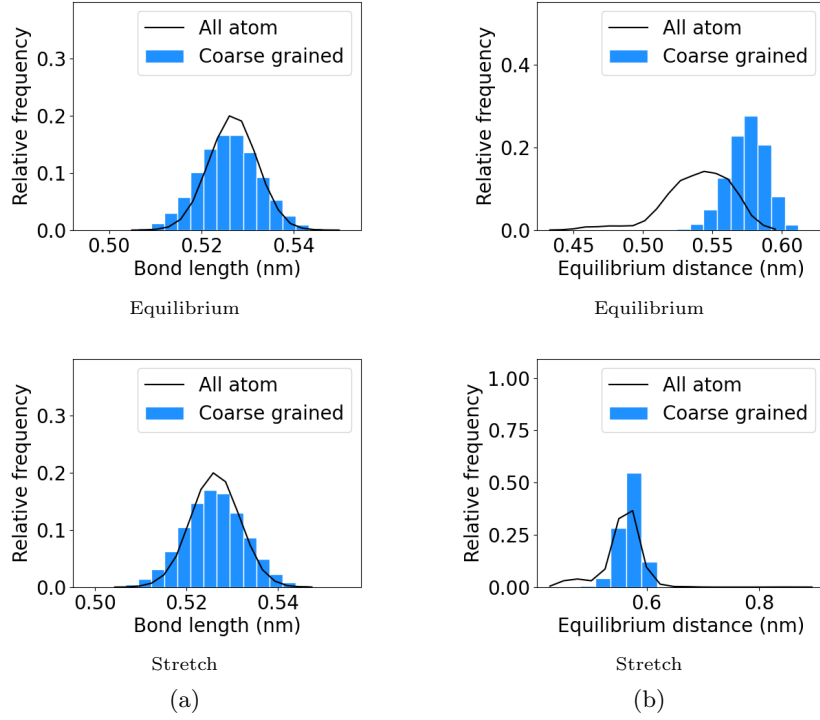


Figure 8: Structural properties. (a) BD geometry parameter distributions between CL1 and CL1 in equilibrium state and stretching progress. (b) NB equilibrium distance distributions between CL1 and CL1 in equilibrium state and stretching progress. (c) RDF of a whole CNC and RDF of a HBonding layer slice or inter HBonding layers slice in equilibrium state. These data confirmed the accurate structural reproduction of CG model in both equilibrium and stretching states.

Table 5: Baselines bonded properties

type	Axial Modulus (GPa)	Persistence Length (nm)			End to end distance (nm)		
		10	20	30	10	20	30
IBI(NVT)	661.6	2.674	4.002	5.785	4.477	8.884	13.141
RE(NVT)	660.9	6.688	5.307	5.069	4.433	8.870	13.315
MARTINI(NPT)	10.7	5.440	5.054	6.807	4.134	8.078	11.907
RL(NPT)	130.5	8.990	10.176	10.106	4.529	9.199	13.432
AA(NPT)	133.5	9.755	9.815	9.716	4.523	9.355	13.536
Error							
IBI(NVT)	396%	73%	59%	40%	1%	5%	3%
RE(NVT)	395%	31%	46%	48%	2%	5%	2%
MARTINI(NPT)	92%	44%	49%	30%	9%	14%	12%
RL(NPT)	2%	8%	4%	4%	0%	2%	1%

Table 6: Baselines nonbonded properties

type	Strength (MPa)			Toughness (GPa)		
	V	H	S	V	H	S
IBI(NVT)	654.5	240.5	495.2	109.3	79.3	334.8
RE(NVT)	833.3	260.9	491.7	87.5	77.6	344.4
MARTINI(NPT)	471.6	268.1	259.7	62.0	396.6	838.7
RL(NPT)	1191.9±6.0	653.5±1.1	509.8±4.6	117.0±3.2	78.1±1.2	166.9±3.8
AA(NPT)	1224.0±9.7	638.2±4.8	467.0±3.7	111.0±2.5	77.9±2.8	190.1±4.6
Error						
IBI(NVT)	47%	62%	6%	2%	2%	76%
RE(NVT)	32%	59%	5%	21%	0%	81%
MARTINI(NPT)	61%	58%	44%	44%	309%	341%
RL(NPT)	3%	2%	9%	5%	0%	12%

3.6 Training without thresholds and training using other optimization methods

The advantages of the thresholds and min in the reward function were proved a parallel training without thresholds and min function were provided, as shown in Figure S17 and S18. The results from parallel training elucidated that the thresholds did not harm best performances and accelerate learning in the early stage.

On the other hand, the parameterization of interaction potentials is similar to the hyperparameter optimization of neural network models. The parameterization of interaction potentials is similar to the hyperparameter optimization of neural network models. To further validate the effectiveness of RL, parallel training using other optimization methods including Tree-structured Parzen Estimator[92] (TPE, an implementation of Bayesian Optimization) and Covariance Matrix Adaptation Evolution Strategy[93] (CMAES) were also performed, which are widely applied for hyperparameter tuning. CMAES and TPE was utilized by the implementation of OPTUNA[94], and both the reward function with/without thresholds are both trained (Figure S19). The comparison emphasized the optimization capability of RL to deal with high nonlinear potential parameterization problems and keep critical stochasticity to compensate for insufficient sampling.

3.7 Additional inspections

Additional inspections of the mechanical properties of the CG model were performed to verify its transferability and generalization to other cases.

3.7.1 Draw-out and Tear-apart

Opening, in-plane shear, and out-of-plane shear are the three types of fracture. The transverse stretch used in training corresponded to the type of opening fracture. For in-plane and out-of-plane shear, the draw-out and tear-apart were tested using steered molecular dynamics(Figure 9). A draw-out test was performed in a periodic cell under the NPT ensemble, and the middle cellulose chain was pulled out of the CNC. A tear-apart test towed the tips of the middle part of the cellulose chains perpendicular to their backbones under the NVT ensemble. The structure and force-displacement curves are shown in Figure 9. Determined by the periodic structure and HBonds of cellulose, draw-out was a periodic process with force fading. The tear-apart test was a type of force-increasing process, and the displacements and maximum forces of the AA and CG simulations are similar. These results indicate that the CG model can accurately illustrate the three types of CNC fracture.

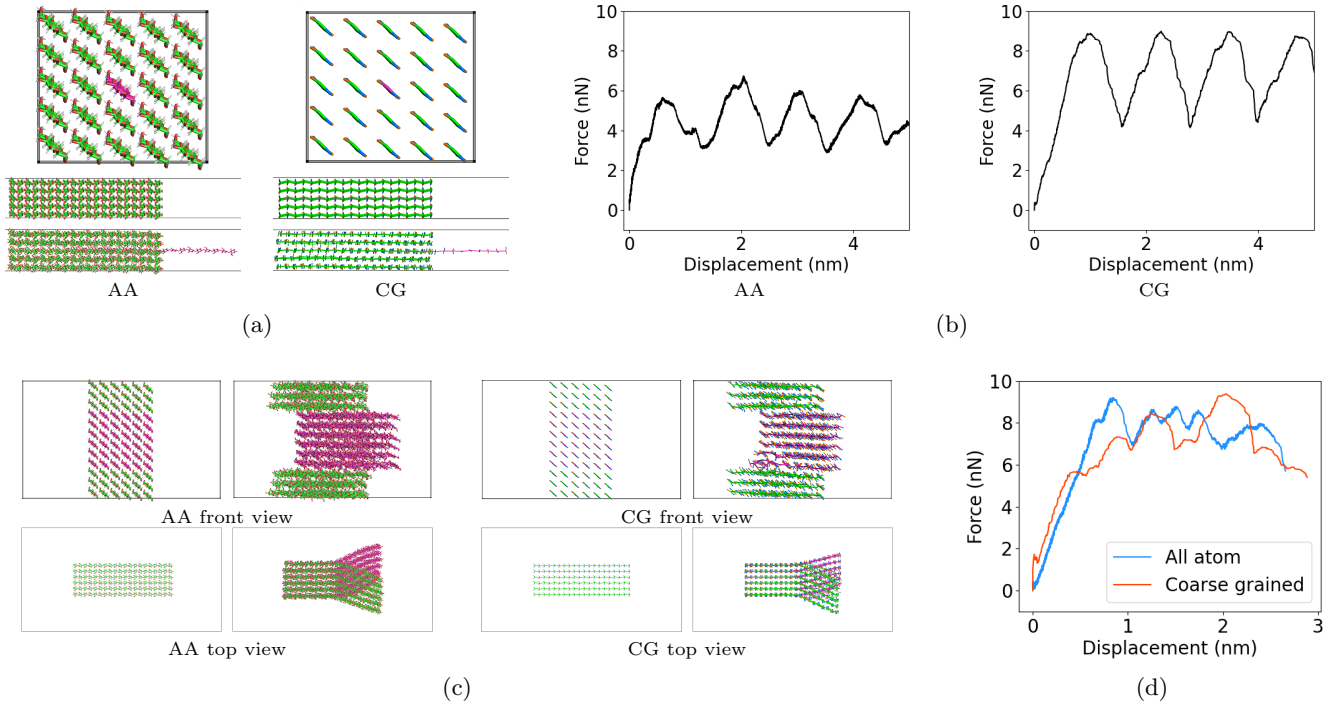


Figure 9: Draw-out and Tear-apart. (a) Draw-out and (b) curves. (c) Tear-apart and (d) curves. The transverse stretch resembled an opening fracture, whereas the in-plane and out-of-plane shear were examined using draw-out and tear-apart simulations, respectively. The draw-out and tear-apart were performed separately under the NPT and NVT ensembles by steered molecular dynamics with axial towing of the middle cellulose chain or perpendicular towing of the middle chains. The force-displacement curve of the draw-out presented periodic fading force curves that were ruled by their structure, whereas the tear-apart force was incremental. The maximum force and frequency of the draw-out and tear-apart matched those of the AA references. Therefore, the CG model can quantitatively represent the in-plane and out-of-plane shear.

3.7.2 Adhesion and Bending

Although our CG model was designed for pure periodic systems, adhesion and bending loads were applied to verify its applicability to aperiodic systems (Figure 10). An adhesion test was performed to determine the adhesion energy of nearby aperiodic CNC in the axial direction. A vertical load was applied at the center point of the cellulose bundle for the bending test. The adhesion energy of the CG model was evidently larger than that of AA, and the slightly lower force of the CG model in bending may result from the BD force constant rescaling of the angles and dihedrals. The results confirmed that the CG model could also be used in aperiodic CNC systems with a slightly lower accuracy.

3.7.3 Transverse arrangement

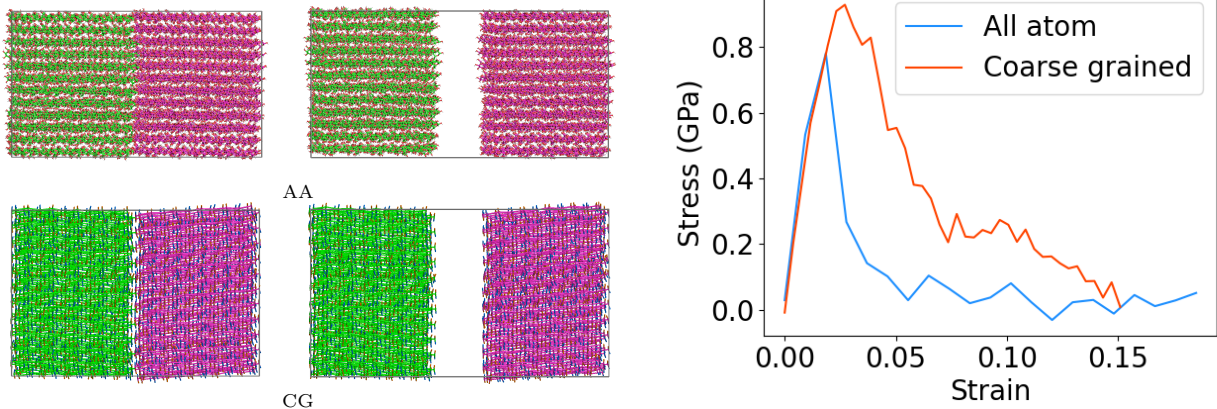
Unlike previous BD directionality CG models[36–39], the CG model was designed to present directionality via branched beads and HBond-like interactions. This makes it possible to consider the transverse arrangements of CNCs with cross and symmetric patterns. The results of the arrangement patterns confirmed that the fractures and performance differed significantly from those of the crystals, as shown in Figure 11. The symmetric pattern was inspired by the twin structure, and the results indicated that this pattern exhibited a better toughness than the crystal. The cross pattern was symmetric in both directions. In these two patterns, frictional sliding was impeded and transformed into local rotations, thereby achieving better toughness and ductility in a symmetric pattern. These results emphasize the importance of the transverse arrangement, which cannot be described by former CG models.

3.7.4 Brick-and-mortar

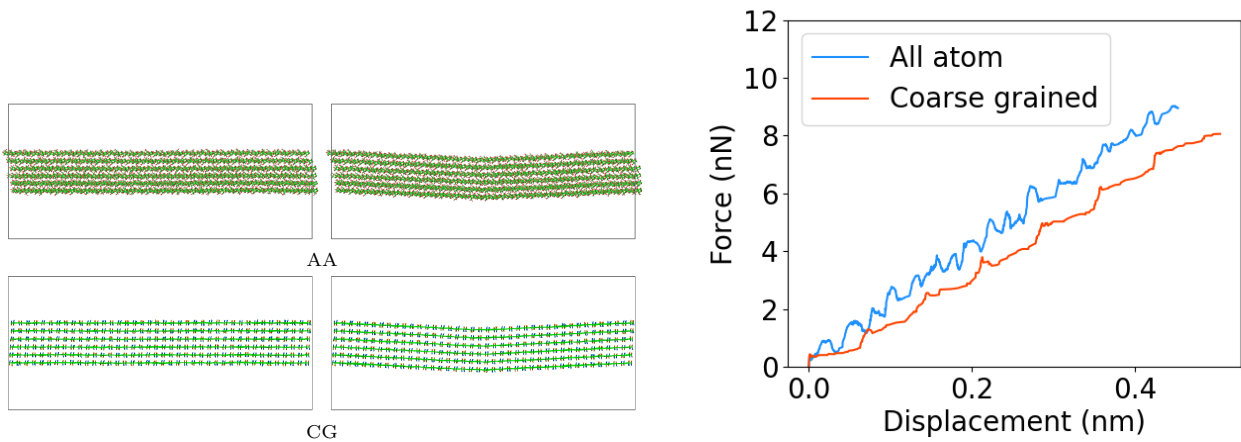
According to previous studies, highly aligned CNCs can be assembled into staggered brick-and-mortar[95, 96] and chiral nematic helicoidal structures[96]. The brick-and-mortar structure can increase the stiffness, strength, and toughness, and this test can be considered as mesoscopic in-plane shear, as shown in Figure 12. In these simulations, each CNC brick was composed of 36 parallel cellulose chains and 4×8 CNCs were assembled. The elementary cellulose chains contained 10, 20, 40, 60 or 80 cellulose residues. There are 1.5 million atoms in the AA system if the elementary brick is 60 cellulose residues long. Longer cellulose bricks were simulated using the CG model only. Local slips and small decentralized slips appeared as frictional fracture behaviors for the staggered structures with different brick lengths. Stretch toughness and overlapping length also demonstrated a positive correlation.

3.7.5 Computational efficiency

The computational efficiencies of the AA and CG models were compared using equilibrium simulations. A sequence of square periodic CNCs (the word square indicates that the row and column numbers of the transverse section of the CNCs



(a)



(b)

Figure 10: Adhesion and Bending in aperiodic systems. (a) Adhesion. Two CNCs were placed tightly close along the chain direction and were clung by the interface adhesion energy. They were then torn away from one another. The adhesion energy of the CG model was larger. (b) Bending. A vertical load was applied at the center of the CNC bundle to induce bending. The force curves of adhesion and bending confirm the capabilities of the CG model in aperiodic systems. Unlike the axial modulus dominated by bonds, the bending is also affected by the angles and dihedrals. The slightly lower bending modulus was assumed to be caused by the rescaling of the angle and dihedral force constants.

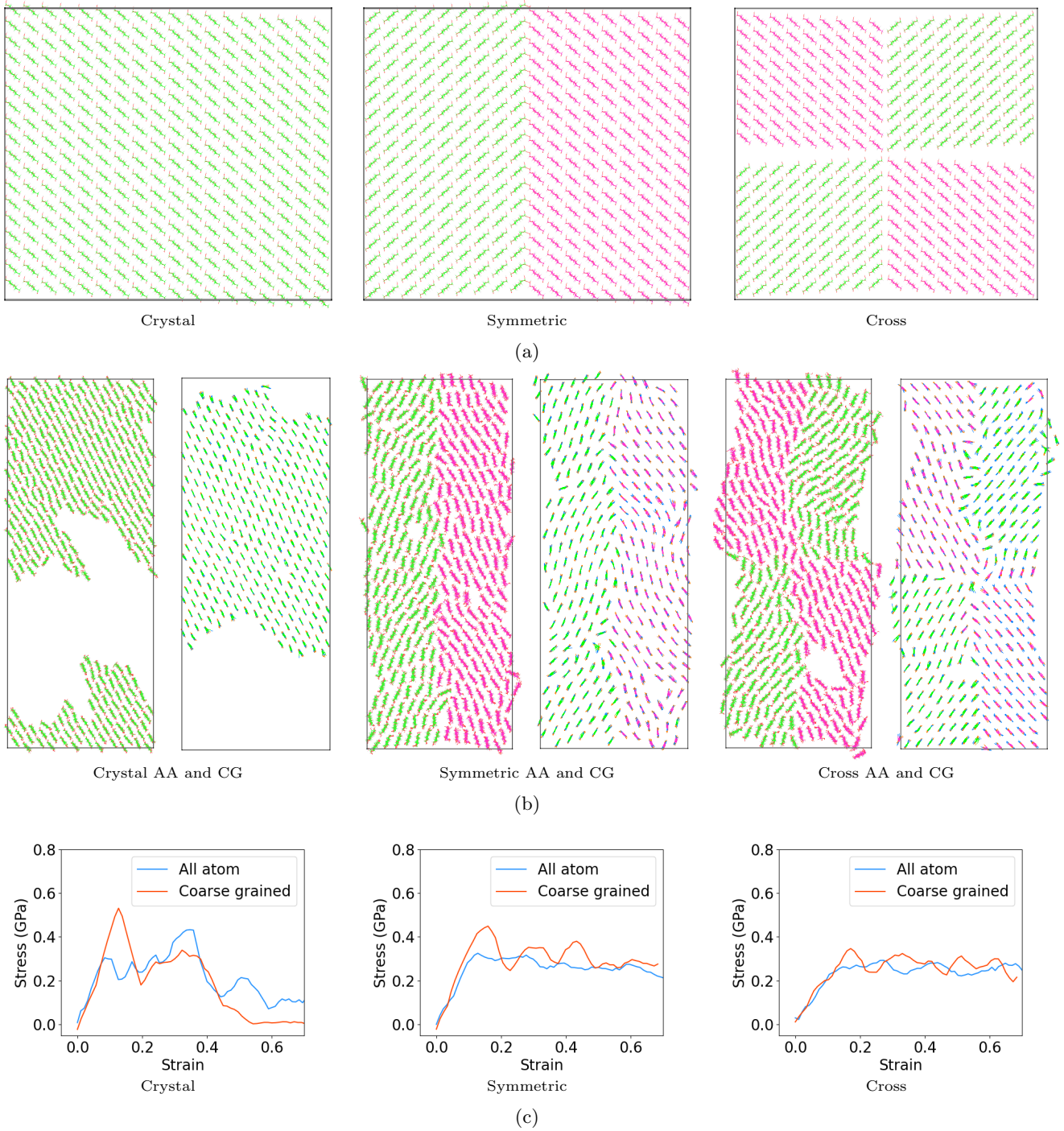


Figure 11: Transverse arrangement. (a) Transverse arrangement patterns. The crystal pattern was the same as that used for the potential parameterization. The symmetric pattern was inspired by the twin structure. The cross pattern was an X-shaped arrangement. (b) AA (left) and CG (right) structures under same vertical strain. In the symmetric and cross patterns, the global stretch was composed of the deformation of units, whose frictional sliding was hampered. In this case, local rotations became the dominant behavior, leading to better toughness and ductility. (c) Stress-strain curves of the three patterns. The transverse arrangements in the symmetric and cross patterns cannot be expressed by previous CG models. These arrangements should be emphasized in future studies.

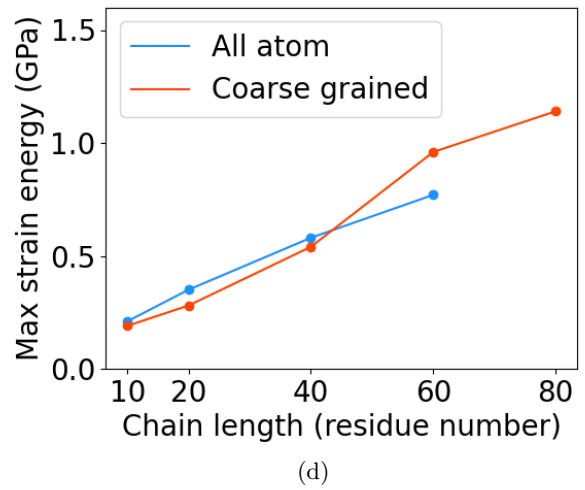
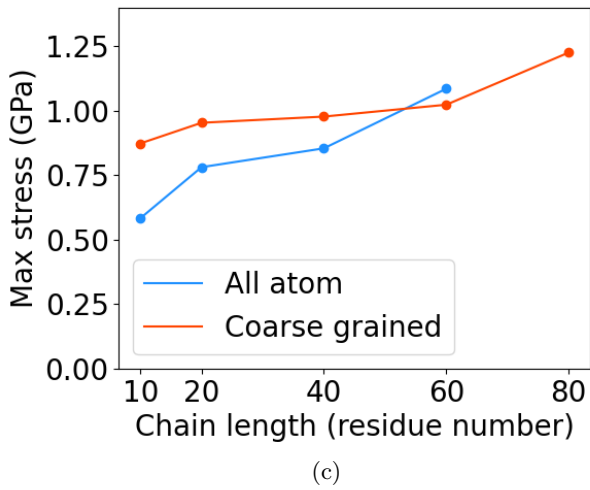


Figure 12: Brick-and-mortar. (a) Brick-and-mortar models and fractures. (b) Stress-strain curves when the elementary cellulose chain length was 40 residues. (c) Strength and (d) toughness curves of different elementary chain lengths. Highly aligned CNCs can assemble into brick-and-mortar structures [95, 96] in the axial direction, and this staggered structure can improve strength and toughness. The brick-and-mortar stretch was also a CNC-level in-plane shear, and was heavily influenced by the length of the elementary cellulose chains. The CG model accurately describes the structural behavior of the brick-and-mortar. The brick-and-mortar fracture was composed of major local slips and decentralized minor slips, and the toughness is positively correlated with the overlapping length.

were the same) equilibrium simulations of different sizes were used, in which the atom number of the AA models ranged from seven kilos to one million. The benchmark simulations were performed using central processing units (CPU) and graphical processing units (GPU). The HB interaction does not support hardware acceleration, and the AA simulations using only the same amount of CPU resources are shown in Figure 13. For the AA and CG simulations using only the CPU, six cores were allocated exclusively to each task. Six cores and an additional exclusive GPU were allocated for the accelerated AA simulations using a GPU. The results confirmed that the CG model was 20 times faster than its AA counterpart when using the same resources. Even when referring to the AA models with additional GPU acceleration, the efficiencies of the CG models were triple. When a GPU-accelerated HB interaction is implemented and tested in the future, its potential can be fully exploited.

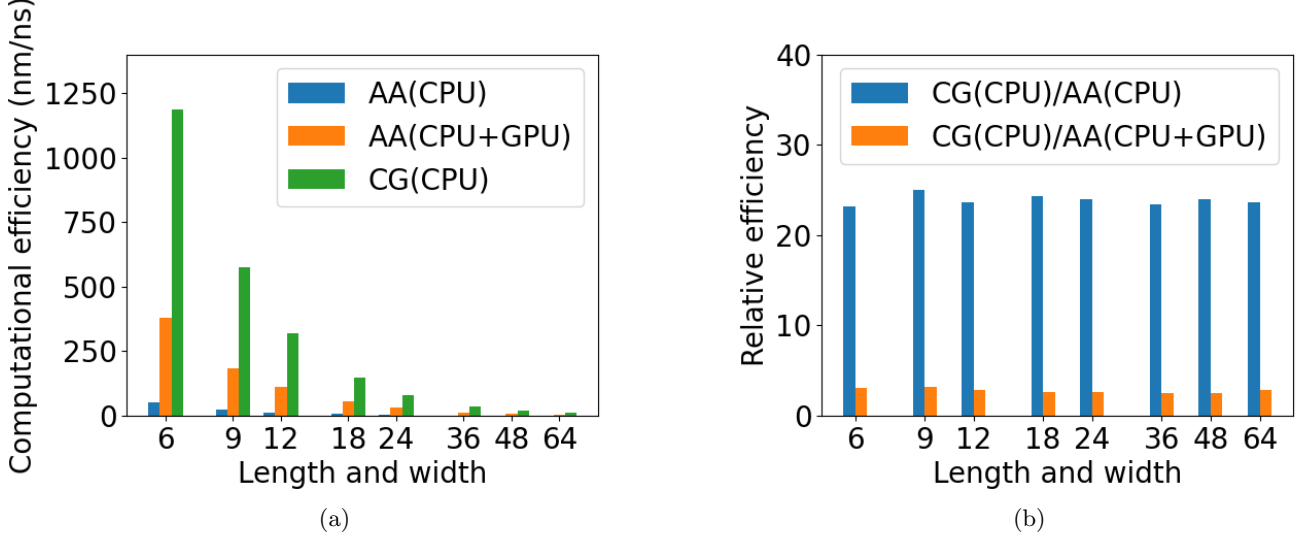


Figure 13: Computation efficiency. (a) efficiency data and (b) relative efficiency data with AA simulations as a baseline. Currently, the HB interactions used does not support hardware acceleration. Referring to the AA simulations with same amount of CPU resources, the CG model was 20 times faster in CNC equilibrium simulations of different transverse sizes. The efficiency of the CG model was still triple when additional exclusive GPU resources were utilized for AA. However, its computational efficiency has not yet been fully proven.

Discussions

Cellulose materials are usually composed of long and thin cellulose nanofibrils, and previous CG models of cellulose have emphasized their axial properties[29, 30]. However, CNCs are anisotropic and much shorter, and their transverse properties should not be disparaged, which is important for future development of cellulose materials. Some exhibit transverse anisotropy using anisotropic particles[26, 35] or additional artificial bonds[36–39], which are still incapable of representing the transverse anisotropy.

The challenges and main characteristics of the CG model include the flat residues and hydrogen bond (HBond) interactions. The CG model could reveal the laminar structures and frictional sliding, which are two critical properties for CNCs transverse anisotropy, and the former CG models could not reflect accurately. Except for the HBond interactions, only the harmonic and Lennard-Jones potentials were included in the BD and NB interactions. This model also confirms the potential parameterization capability of RL; only a discriminant reward function was required. The reward function for RL includes the matching degree of the BD properties (axial modulus and polymer stiffness) and the NB properties (transverse strength and toughness). RL may be more widely applied to potential parameterizations in the future.

In the context of CG modeling, this model owns its uniqueness. In principle, it followed bottom-up approach starting from molecular details but used strength and toughness as optimization target, rather than potential of mean force or other structural distributions. And it chose simple analytical function form, which is also similar to top-down to a certain extent. Its mapping and topology restores molecular shape and frictions, and the interaction functions implemented anisotropic HBonding. And more importantly, it was designed to explore equilibrium states and processes involving dynamics properties with quantitative accuracy. On the other hand, this model preserved necessary molecular structures, and may be suitable for AA reconstruction based upon CG models.

However, several problems are encountered in the CG model. The first is the rescale of the angle and dihedral interaction force constants. The CG model, which has significantly fewer degrees of freedom, must compensate for the polymer stiffness properties by decreasing the force constants (Table S4). The former CG model addressing persistence length did not require a precise match (40 nm)[34]. Some studies also estimated the persistence length of a bundle of cellulose chains instead of a single free chain[97]. These smaller force constants may cause problems for other properties involving the angles and dihedrals. For example, a lower stress was observed during the bending test.

The nonbonded equilibrium distances are also problematic. The equilibrium distances of the CG model were larger than those of their AA counterparts (Figure S12, Figure S13), and the enlargement of the CL2-CL3 NB distance coefficients was determined using RL (Figure 5). This means that the distance coefficients and equilibrium distances do not correspond to

the well-relaxed AA equilibrium distances or radial distribution function. In this study, the equilibrium distance of a pair was defined as the average minimum distance. Nearly all minimum distances of pairs are from beads of nearby HBonding layers; only the minimum distances of CL2-CL3 are from beads in the same HBonding layer. Therefore, we infer that the equilibrium distances from nearby HBonding plane pairs are appropriate estimations of σ values for the LJ potentials because the dominant NB interactions are HBonds in the HBonding layers. The overall enlargement of the NB distance coefficients is assumed to be required by the increased σ_{p23} to retain the crystal structure. Moreover, the enlargement of σ_{p23} may be an assimilation of σ because the equilibrium distance between CL2 and CL3 is the smallest. The Phenomenon of frictional sliding may be presented more easily if all σ values are close to each other. This also influenced the accuracy of θ_0 in the HB potential. In the first reduction, the distance coefficients between pairs of same kinds were artificially aligned to be the same because laminar structure and coefficients are critical for CG model. To align with the artifacts constraints, θ_0 in the HB potential was determined by the mapped artificial model, which was constructed by coordinate offset and ideally parallel. Thus, the θ_0 is an approximation without strong theory background.

Other minor problems also exist. Our model may not perform well in aperiodic cellulose systems (as in the adhesion test). The pressure curve of the CG model under the NPT ensemble exhibited a larger oscillation amplitude. Otherwise, some molecular details were ignored in the CG model. For instance, the rotational degrees of freedom of the hydrogen atoms on the branch hydroxyls were neglected in harmonic BD potentials (Figure S20). Moreover, one technical problem temporarily restrained the application potential of the CG model: the HBond-like pair style does not support hardware acceleration. Therefore, the computational efficiency of the CG model has not yet been fully realized.

As a pioneering work that introduced HBonds, the CG model of CNC could promote further research. The development of cellulose CG models has mainly focused on the native cellulose. However, solvent environments, particularly humidity, are key factors for cellulose materials[34, 98–100] and are not well represented in cellulose CG models[30]. Chemical surface modifications and interactions with other molecules such as hemicellulose or lignin are also critical for enhancing the performance of cellulose materials. These problems are strongly dependent on the hydroxyls of cellulose residues. Regarding the computational resources and expertise, these interactions were not considered in this study. With the help of HBond-like interactions, a later CG model could attempt to present more properties of the cellulose. We hope that this model will facilitate future development of CG models.

As an application of RL for potential parameterization, our methods and implementations are not heavily dependent on cellulose, and may help in later CG model development. In the CG model, much priori knowledge, including pre-defined mapping and interaction potential expressions, is used to reduce the difficulty and enhance physical explainability. However, the resultant effect of priori knowledge is uncertain. Fully automatic optimization may achieve models with better performances. Transfer Learning and Imitation Learning methods may also be applied in the future to further accelerate RL in the potential parameterization applications.

Conclusions

In this study, we introduce a novel CG cellulose model with explicit branch beads and HBond-like interactions that can reproduce the anisotropy of cellulose nanocrystals. The strength and toughness in the three characteristic directions of the orthotropic transverse section were quantitatively reproduced without anisotropic particles or additional bonds. This study is a pioneering work that applied degenerate RL as a nonlinear optimizer to perform direct analytical potential parameterization, and the physical meanings were enhanced by integrating the Boltzmann inversion method. This model may also contribute to the CG modeling in its own way. Rather than targeting at traditional mapped structural distributions, this CG model extended bottom-up approach by implementing anisotropic interactions and hydrogen bonding and incorporating mechanical properties. The obvious advantage is the simple analytical function forms supported by optimized mapping and topology that explore dynamics properties quantitatively. It is a hybrid-hybrid model: combing bottom-up and top-down, considering both equilibrium and non-equilibrium. Such a not too coarse model may also benefit multi-scale simulations which requires backmapping and reconstruction. This model synthesizes physical knowledge, traditional modeling, and Machine Learning methods. It aids in the understanding of the importance of hydrogen bonds and the transverse anisotropy. With an appropriate reward function based on the target properties and statistics-guided reduction, the RL agent can determine the appropriate coefficients without consuming considerable computational resources. The target anisotropic properties considered included the bonded properties (axial elastic modulus and polymer stiffness) and nonbonded properties (transverse stretch strength and toughness), all of which were accurately matched with errors below 15%. Several additional inspections were performed after the training, including in-plane shear, out-of-plane shear, adhesion energy, bending, transverse arrangement, and brick-and-mortar structures. The transferability and generalization of this CG model were proven through additional inspections. These results emphasize that transverse anisotropy is important for transverse arrangements, which has not been quantitatively captured in previous CG models. Two transverse arrangement patterns with improved toughness and ductility were introduced. We found a positive correlation between the overlapping length and toughness of the brick-and-mortar structures. Data on transverse arrangements and brick-and-mortar structures may aid advanced material design in the future. This model may also aid in addressing interactions between cellulose and other polar molecules on a mesoscopic scale. This study emphasizes that Machine Learning can also be applied to construct effective analytical potentials that are better in terms of explainability, transferability, and kinetics. Although our results demonstrate the efficiency of RL, many refinements remain to be explored, particularly for molecular systems. For example, the necessity of inspiration from human knowledge and traditional methods such as Boltzmann inversion is still unclear. Finally, our basic parameterization approach is general to the applications, implying that our workflow may also

be applicable to other molecular systems. Transfer Learning and Imitation Learning methods may also be integrated with RL to solve similar problems in the future.

Conflict of Interest declaration

The author declares no competing financial interest.

Data availability

- The modified hbond/dreiding/lj/angleoffset was merged into the official LAMMPS EXTRA-MOLECULE at <https://github.com/lammps/lammps>
- The codes for potential parameterization training are available at <https://github.com/EiPiFun/rl-cll-cg>
- The training data, models, simulation codes, processed data and plot scripts are available at <https://github.com/EiPiFun/rl-cll-cg-data>
- The raw data, pre-processing codes, and post-processing codes are available upon requests.

Acknowledgments

Xu Dong thanks the Department of Engineering Mechanics of Zhejiang University for the funding and computational resources.

Author Contributions

Xu Dong: Conceptualization, Data curation, Formal analysis, Investigation, Methodology, Project administration, Resources, Software, Validation, Visualization, Writing - original draft, Writing - review & editing.

A professor from the Department of Engineering Mechanics of Zhejiang University provided some additional Methodology, Resources, and Writing - review & editing helps and chose to be anonymous.

References

- [1] Robert J Moon, Gregory T Schueneman, and John Simonsen. Overview of cellulose nanomaterials, their capabilities and applications. *Jom*, 68:2383–2394, 2016.
- [2] Joo-Hyung Kim, Bong Sup Shim, Heung Soo Kim, Young-Jun Lee, Seung-Ki Min, Daseul Jang, Zafar Abas, and Jaehwan Kim. Review of nanocellulose for sustainable future materials. *International Journal of Precision Engineering and Manufacturing-Green Technology*, 2:197–213, 2015.
- [3] Hwee Li Teo and Roswanira Abdul Wahab. Towards an eco-friendly deconstruction of agro-industrial biomass and preparation of renewable cellulose nanomaterials: A review. *International Journal of Biological Macromolecules*, 161:1414–1430, 2020.
- [4] Robert J Moon, Ashlie Martini, John Nairn, John Simonsen, and Jeff Youngblood. Cellulose nanomaterials review: structure, properties and nanocomposites. *Chemical Society Reviews*, 40(7):3941–3994, 2011.
- [5] Qianqian Zhu, Simeng Liu, Jianzhong Sun, Jun Liu, C Joseph Kirubakaran, Honglei Chen, Weihua Xu, and Qianqian Wang. Stimuli-responsive cellulose nanomaterials for smart applications. *Carbohydrate Polymers*, 235:115933, 2020.
- [6] Haishun Du, Wei Liu, Miaomiao Zhang, Chuanling Si, Xinyu Zhang, and Bin Li. Cellulose nanocrystals and cellulose nanofibrils based hydrogels for biomedical applications. *Carbohydrate polymers*, 209:130–144, 2019.
- [7] Jiwoo Yu, Aurelia C Wang, Mingyue Zhang, and Zhiqun Lin. Water treatment via non-membrane inorganic nanoparticles/cellulose composites. *Materials Today*, 50:329–357, 2021.
- [8] Huayu Liu, Haishun Du, Ting Zheng, Kun Liu, Xingxiang Ji, Ting Xu, Xinyu Zhang, and Chuanling Si. Cellulose based composite foams and aerogels for advanced energy storage devices. *Chemical Engineering Journal*, 426:130817, 2021.
- [9] Yang Wang, Lina Zhang, Jinping Zhou, and Ang Lu. Flexible and transparent cellulose-based ionic film as a humidity sensor. *ACS Applied Materials & Interfaces*, 12(6):7631–7638, 2020.
- [10] Davi Texeira Reis, Igor Hernandes Santos Ribeiro, and Douglas Henrique Pereira. Dft study of the application of polymers cellulose and cellulose acetate for adsorption of metal ions (cd 2+, cu 2+ and cr 3+) potentially toxic. *Polymer Bulletin*, 77:3443–3456, 2020.
- [11] Chuantao Zhu, Susanna Monti, and Aji P Mathew. Evaluation of nanocellulose interaction with water pollutants using nanocellulose colloidal probes and molecular dynamic simulations. *Carbohydrate polymers*, 229:115510, 2020.
- [12] Pan Chen, Yu Ogawa, Yoshiharu Nishiyama, Ahmed E Ismail, and Karim Mazeau. Linear, nonlinear and plastic bending deformation of cellulose nanocrystals. *Physical Chemistry Chemical Physics*, 18(29):19880–19887, 2016.
- [13] Imke Diddens, Bridget Murphy, Michael Krisch, and Martin Muller. Anisotropic elastic properties of cellulose measured using inelastic x-ray scattering. *Macromolecules*, 41(24):9755–9759, 2008.

- [14] Shinichiro Iwamoto, Weihua Kai, Akira Isogai, and Tadahisa Iwata. Elastic modulus of single cellulose microfibrils from tunicate measured by atomic force microscopy. *Biomacromolecules*, 10(9):2571–2576, 2009.
- [15] Ryan Wagner, Robert J Moon, and Arvind Raman. Mechanical properties of cellulose nanomaterials studied by contact resonance atomic force microscopy. *Cellulose*, 23:1031–1041, 2016.
- [16] Fernando L Dri, Louis G Hector, Robert J Moon, and Pablo D Zavattieri. Anisotropy of the elastic properties of crystalline cellulose $i\beta$ from first principles density functional theory with van der waals interactions. *Cellulose*, 20:2703–2718, 2013.
- [17] Xiawa Wu, Robert J Moon, and Ashlie Martini. Tensile strength of $i\beta$ crystalline cellulose predicted by molecular dynamics simulation. *Cellulose*, 21:2233–2245, 2014.
- [18] Qinghua Meng, Bo Li, Teng Li, and Xi-Qiao Feng. Effects of nanofiber orientations on the fracture toughness of cellulose nanopaper. *Engineering Fracture Mechanics*, 194:350–361, 2018.
- [19] Qinghua Meng, Bo Li, Teng Li, and Xi-Qiao Feng. A multiscale crack-bridging model of cellulose nanopaper. *Journal of the Mechanics and Physics of Solids*, 103:22–39, 2017.
- [20] Tongye Shen and S Gnanakaran. The stability of cellulose: a statistical perspective from a coarse-grained model of hydrogen-bond networks. *Biophysical journal*, 96(8):3032–3040, 2009.
- [21] Cyrus Djahedi, Malin Bergenstr hle-Wohlert, Lars A Berglund, and Jakob Wohlert. Role of hydrogen bonding in cellulose deformation: the leverage effect analyzed by molecular modeling. *Cellulose*, 23:2315–2323, 2016.
- [22] Malin Wohlert, Tobias Bensefelt, Lars W gberg, Istv n Fur , Lars A Berglund, and Jakob Wohlert. Cellulose and the role of hydrogen bonds: not in charge of everything. *Cellulose*, pages 1–23, 2022.
- [23] Xiawa Wu, Robert J Moon, and Ashlie Martini. Atomistic simulation of frictional sliding between cellulose $i\beta$ nanocrystals. *Tribology Letters*, 52:395–405, 2013.
- [24] Chi Zhang, Sinan Ketten, Dominique Derome, and Jan Carmeliet. Hydrogen bonds dominated frictional stick-slip of cellulose nanocrystals. *Carbohydrate Polymers*, 258:117682, 2021.
- [25] Aleksandar Y Mehandzhiyski and Igor Zozoulenko. A review of cellulose coarse-grained models and their applications. *Polysaccharides*, 2(2):257–270, 2021.
- [26] Nicolas Rolland, Aleksandar Y Mehandzhiyski, Mohit Garg, Mathieu Linares, and Igor V Zozoulenko. New patchy particle model with anisotropic patches for molecular dynamics simulations: Application to a coarse-grained model of cellulose nanocrystal. *Journal of Chemical Theory and Computation*, 16(6):3699–3711, 2020.
- [27] Aleksandar Y Mehandzhiyski, Nicolas Rolland, Mohit Garg, Jakob Wohlert, Mathieu Linares, and Igor Zozoulenko. A novel supra coarse-grained model for cellulose. *Cellulose*, 27:4221–4234, 2020.
- [28] Zhaofan Li and Wenjie Xia. Coarse-grained modeling of nanocellulose network towards understanding the mechanical performance. *Extreme Mechanics Letters*, 40:100942, 2020.
- [29] Xin Qin, Shizhe Feng, Zhaoxu Meng, and Sinan Ketten. Optimizing the mechanical properties of cellulose nanopaper through surface energy and critical length scale considerations. *Cellulose*, 24:3289–3299, 2017.
- [30] Upamanyu Ray, Zhenqian Pang, and Teng Li. Mechanics of cellulose nanopaper using a scalable coarse-grained modeling scheme. *Cellulose*, 28(6):3359–3372, 2021.
- [31] Cesar A Lopez, Giovanni Bellesia, Antonio Redondo, Paul Langan, Shishir PS Chundawat, Bruce E Dale, Siewert J Marrink, and S Gnanakaran. Martini coarse-grained model for crystalline cellulose microfibrils. *The Journal of Physical Chemistry B*, 119(2):465–473, 2015.
- [32] Lintao Bu, Gregg T Beckham, Michael F Crowley, Christopher H Chang, James F Matthews, Yannick J Bomble, William S Adney, Michael E Himmel, and Mark R Nimlos. The energy landscape for the interaction of the family 1 carbohydrate-binding module and the cellulose surface is altered by hydrolyzed glycosidic bonds. *The Journal of Physical Chemistry B*, 113(31):10994–11002, 2009.
- [33] Jakob Wohlert and Lars A Berglund. A coarse-grained model for molecular dynamics simulations of native cellulose. *Journal of Chemical Theory and Computation*, 7(3):753–760, 2011.
- [34] Srinivas Goundla, Cheng Xiaolin, et al. Coarse-grain model for natural cellulose fibrils in explicit water. 2014.
- [35] Huong TL Nguyen and David M Huang. Systematic bottom-up molecular coarse-graining via force and torque matching using anisotropic particles. *The Journal of Chemical Physics*, 156(18), 2022.
- [36] Bingxin Fan and Janna K Maranas. Coarse-grained simulation of cellulose $i\beta$ with application to long fibrils. *Cellulose*, 22:31–44, 2015.
- [37] Majid G Ramezani and Behnoush Golchinfar. Mechanical properties of cellulose nanocrystal (cnc) bundles: Coarse-grained molecular dynamic simulation. *Journal of Composites Science*, 3(2):57, 2019.
- [38] Mehdi Shishehbor and Pablo D Zavattieri. Effects of interface properties on the mechanical properties of bio-inspired cellulose nanocrystal (cnc)-based materials. *Journal of the Mechanics and Physics of Solids*, 124:871–896, 2019.
- [39] Mehdi Shishehbor, Hyeyoung Son, Md Nuruddin, Jeffrey P Youngblood, Chelsea Davis, and Pablo D Zavattieri. Influence of alignment and microstructure features on the mechanical properties and failure mechanisms of cellulose nanocrystals (cnc) films. *Journal of the Mechanical Behavior of Biomedical Materials*, 118:104399, 2021.
- [40] Frank No , Alexandre Tkatchenko, Klaus-Robert M ller, and Cecilia Clementi. Machine learning for molecular simulation. *Annual Review of Physical Chemistry*, 71(1):361–390, 2020.
- [41] Raidel Martin-Barrios, Edisel Navas-Conyedo, Xuyi Zhang, Yunwei Chen, and Jorge Gul n-Gonz lez. An overview about neural networks potentials in molecular dynamics simulation. *International Journal of Quantum Chemistry*, 124(11):e27389, 2024.

- [42] Wojciech Samek, Grégoire Montavon, Sebastian Lapuschkin, Christopher J Anders, and Klaus-Robert Müller. Explaining deep neural networks and beyond: A review of methods and applications. *Proceedings of the IEEE*, 109(3):247–278, 2021.
- [43] Rohit Batra and Subramanian Sankaranarayanan. Machine learning for multi-fidelity scale bridging and dynamical simulations of materials. *Journal of Physics: Materials*, 3(3):031002, 2020.
- [44] Bridgette J Befort, Ryan S DeFever, Garrett M Tow, Alexander W Dowling, and Edward J Maginn. Machine learning directed optimization of classical molecular modeling force fields. *Journal of Chemical Information and Modeling*, 61(9):4400–4414, 2021.
- [45] Jesse M Sestito, Mary L Thatcher, Leshi Shu, Tequila AL Harris, and Yan Wang. Coarse-grained force field calibration based on multiobjective bayesian optimization to simulate water diffusion in poly- ϵ -caprolactone. *The Journal of Physical Chemistry A*, 124(24):5042–5052, 2020.
- [46] Ke Duan, Yonglyu He, Yijun Li, Jiahuan Liu, Junjie Zhang, Yujin Hu, Rongming Lin, Xuelin Wang, Weiming Deng, and Li Li. Machine-learning assisted coarse-grained model for epoxies over wide ranges of temperatures and cross-linking degrees. *Materials and Design*, 183, 2019.
- [47] Henry Chan, Mathew J Cherukara, Badri Narayanan, Troy D Loeffler, Chris Benmore, Stephen K Gray, and Subramanian KRS Sankaranarayanan. Machine learning coarse grained models for water. *Nature communications*, 10(1):379, 2019.
- [48] M Razi, A Narayan, RM Kirby, and D Bedrov. Force-field coefficient optimization of coarse-grained molecular dynamics models with a small computational budget. *Computational Materials Science*, 176:109518, 2020.
- [49] Anirban Chandra, Troy Loeffler, Henry Chan, Xiaoyu Wang, GB Stephenson, Michael J Servis, and Subramanian KRS Sankaranarayanan. Reinforcement learning based hybrid bond-order coarse-grained interatomic potentials for exploring mesoscale aggregation in liquid–liquid mixtures. *The Journal of Chemical Physics*, 159(2), 2023.
- [50] Shenghao Wu, Tianyi Liu, Zhirui Wang, Wen Yan, and Yingxiang Yang. Rlrg: When reinforcement learning meets coarse graining. In *NurIPS 2022 AI for Science: Progress and Promises*, 2022.
- [51] Sukriti Manna, Troy D Loeffler, Rohit Batra, Suvo Banik, Henry Chan, Bilvin Varughese, Kiran Sasikumar, Michael Sternberg, Tom Peterka, Mathew J Cherukara, et al. Learning in continuous action space for developing high dimensional potential energy models. *Nature communications*, 13(1):368, 2022.
- [52] Benjamin Recht. A tour of reinforcement learning: The view from continuous control. *Annual Review of Control, Robotics, and Autonomous Systems*, 2(1):253–279, 2019.
- [53] Xuhan Liu, Jun Zhang, Zhonghuai Hou, Yi Isaac Yang, and Yi Qin Gao. From predicting to decision making: Reinforcement learning in biomedicine. *Wiley Interdisciplinary Reviews: Computational Molecular Science*, 14(4):e1723, 2024.
- [54] William G Noid, Ryan J Szukalo, Katherine M Kidder, and Maria C Lesniewski. Rigorous progress in coarse-graining. *Annual review of physical chemistry*, 75(1):21–45, 2024.
- [55] Jaehyeok Jin, Alexander J Pak, Aleksander EP Durumeric, Timothy D Loose, and Gregory A Voth. Bottom-up coarse-graining: Principles and perspectives. *Journal of chemical theory and computation*, 18(10):5759–5791, 2022.
- [56] Sebastian Kmiecik, Dominik Gront, Michal Kolinski, Lukasz Wieteska, Aleksandra Elzbieta Dawid, and Andrzej Kolinski. Coarse-grained protein models and their applications. *Chemical reviews*, 116(14):7898–7936, 2016.
- [57] Thomas Dannenhoffer-Lafage, Jacob W Wagner, Aleksander EP Durumeric, and Gregory A Voth. Compatible observable decompositions for coarse-grained representations of real molecular systems. *The Journal of chemical physics*, 151(13), 2019.
- [58] Nicholas JH Dunn, Thomas T Foley, and William G Noid. Van der waals perspective on coarse-graining: Progress toward solving representability and transferability problems. *Accounts of Chemical Research*, 49(12):2832–2840, 2016.
- [59] Jaehyeok Jin, Alexander J Pak, and Gregory A Voth. Understanding missing entropy in coarse-grained systems: Addressing issues of representability and transferability. *The journal of physical chemistry letters*, 10(16):4549–4557, 2019.
- [60] Margaret E Johnson, Teresa Head-Gordon, and Ard A Louis. Representability problems for coarse-grained water potentials. *The Journal of chemical physics*, 126(14), 2007.
- [61] Jacob W Wagner, James F Dama, Aleksander EP Durumeric, and Gregory A Voth. On the representability problem and the physical meaning of coarse-grained models. *The Journal of chemical physics*, 145(4), 2016.
- [62] William George Noid. Perspective: Coarse-grained models for biomolecular systems. *The Journal of chemical physics*, 139(9), 2013.
- [63] Paulo CT Souza, Riccardo Alessandri, Jonathan Barnoud, Sebastian Thallmair, Ignacio Faustino, Fabian Grünewald, Ilias Patmanidis, Haleh Abdizadeh, Bart MH Bruininks, Tsjerk A Wassenaar, et al. Martini 3: a general purpose force field for coarse-grained molecular dynamics. *Nature methods*, 18(4):382–388, 2021.
- [64] Florian Müller-Plathe. Coarse-graining in polymer simulation: from the atomistic to the mesoscopic scale and back. *ChemPhysChem*, 3(9):754–769, 2002.
- [65] M Scott Shell. The relative entropy is fundamental to multiscale and inverse thermodynamic problems. *The Journal of chemical physics*, 129(14), 2008.
- [66] Sergei Izvekov and Gregory A Voth. A multiscale coarse-graining method for biomolecular systems. *The Journal of Physical Chemistry B*, 109(7):2469–2473, 2005.
- [67] Fabian Grunewald, Mats H Punt, Elizabeth E Jefferys, Petteri A Vainikka, Melanie König, Valtteri Virtanen, Travis A Meyer, Weria Pezeshkian, Adam J Gormley, Maarit Karonen, et al. Martini 3 coarse-grained force field for carbohydrates. *Journal of Chemical Theory and Computation*, 18(12):7555–7569, 2022.
- [68] Goundla Srinivas, Xiaolin Cheng, and Jeremy C Smith. A solvent-free coarse grain model for crystalline and amorphous cellulose fibrils. *Journal of chemical theory and computation*, 7(8):2539–2548, 2011.

- [69] Aidan P Thompson, H Metin Aktulga, Richard Berger, Dan S Bolintineanu, W Michael Brown, Paul S Crozier, Pieter J In't Veld, Axel Kohlmeyer, Stan G Moore, Trung Dac Nguyen, et al. Lammmps-a flexible simulation tool for particle-based materials modeling at the atomic, meso, and continuum scales. *Computer physics communications*, 271:108171, 2022.
- [70] Stephen L Mayo, Barry D Olafson, and William A Goddard. Dreiding: a generic force field for molecular simulations. *Journal of Physical Chemistry*, 94(26):8897–8909, 1990.
- [71] Sakib Matin, Alice EA Allen, Justin Smith, Nicholas Lubbers, Ryan B Jadrach, Richard Messerly, Benjamin Nebgen, Ying Wai Li, Sergei Tretiak, and Kipton Barros. Machine learning potentials with the iterative boltzmann inversion: training to experiment. *Journal of Chemical Theory and Computation*, 20(3):1274–1281, 2024.
- [72] Aditi Khot and Brett M Savoie. δ -learning applied to coarse-grained homogeneous liquids. *The Journal of Chemical Physics*, 159(5), 2023.
- [73] Wujie Wang, Zhenghao Wu, Johannes CB Dietschreit, and Rafael Gómez-Bombarelli. Learning pair potentials using differentiable simulations. *The Journal of Chemical Physics*, 158(4), 2023.
- [74] Valentina Tozzini, Joanna Trylska, Chia-en Chang, and J Andrew McCammon. Flap opening dynamics in hiv-1 protease explored with a coarse-grained model. *Journal of structural biology*, 157(3):606–615, 2007.
- [75] Victor Rühle, Christoph Junghans, Alexander Lukyanov, Kurt Kremer, and Denis Andrienko. Versatile object-oriented toolkit for coarse-graining applications. *Journal of chemical theory and computation*, 5(12):3211–3223, 2009.
- [76] Jonathan Viquerat, Jean Rabault, Alexander Kuhnle, Hassan Ghraieb, Aurélien Larcher, and Elie Hachem. Direct shape optimization through deep reinforcement learning. *Journal of Computational Physics*, 428:110080, 2021.
- [77] Tuomas Haarnoja, Aurick Zhou, Pieter Abbeel, and Sergey Levine. Soft actor-critic: Off-policy maximum entropy deep reinforcement learning with a stochastic actor. In *International conference on machine learning*, pages 1861–1870. Pmlr, 2018.
- [78] Antonin Raffin, Ashley Hill, Adam Gleave, Anssi Kanervisto, Maximilian Ernestus, and Noah Dormann. Stable-baselines3: Reliable reinforcement learning implementations. *Journal of Machine Learning Research*, 22(268):1–8, 2021.
- [79] Noam Razin, Zixuan Wang, Hubert Strauss, Stanley Wei, Jason D Lee, and Sanjeev Arora. What makes a reward model a good teacher? an optimization perspective. *arXiv preprint arXiv:2503.15477*, 2025.
- [80] Mark James Abraham, Teemu Murtola, Roland Schulz, Szilárd Páll, Jeremy C Smith, Berk Hess, and Erik Lindahl. Gromacs: High performance molecular simulations through multi-level parallelism from laptops to supercomputers. *SoftwareX*, 1:19–25, 2015.
- [81] Par Bjelkmar, Per Larsson, Michel A Cuendet, Berk Hess, and Erik Lindahl. Implementation of the charmm force field in gromacs: analysis of protein stability effects from correction maps, virtual interaction sites, and water models. *Journal of chemical theory and computation*, 6(2):459–466, 2010.
- [82] Jing Huang and Alexander D MacKerell Jr. Charmm36 all-atom additive protein force field: Validation based on comparison to nmr data. *Journal of Computational Chemistry*, 34(25):2135–2145, 2013.
- [83] Jing Huang, Sarah Rauscher, Grzegorz Nawrocki, Ting Ran, Michael Feig, Bert L De Groot, Helmut Grubmüller, and Alexander D MacKerell Jr. Charmm36m: an improved force field for folded and intrinsically disordered proteins. *Nature Methods*, 14(1):71–73, 2017.
- [84] Sunhwan Jo, Taehoon Kim, Vidyashankara G Iyer, and Wonpil Im. Charmm-gui: a web-based graphical user interface for charmm. *Journal of Computational Chemistry*, 29(11):1859–1865, 2008.
- [85] Jumin Lee, Xi Cheng, Sunhwan Jo, Alexander D MacKerell, Jeffery B Klauda, and Wonpil Im. Charmm-gui input generator for namd, gromacs, amber, openmm, and charmm/openmm simulations using the charmm36 additive force field. *Biophysical journal*, 110(3):641a, 2016.
- [86] Robert Sinko, Shawn Mishra, Luis Ruiz, Nick Brandis, and Sinan Ketten. Dimensions of biological cellulose nanocrystals maximize fracture strength. *ACS Macro Letters*, 3(1):64–69, 2014.
- [87] Mark A Hilton, Harris W Manning, Ireneusz Górnaiak, Sonia K Brady, Madeline M Johnson, Jochen Zimmer, and Matthew J Lang. Single-molecule investigations of single-chain cellulose biosynthesis. *Proceedings of the National Academy of Sciences*, 119(40):e2122770119, 2022.
- [88] Loes MJ Kroon-Batenburg, Peter H Kruiskamp, Johannes FG Vliegthart, and Jan Kroon. Estimation of the persistence length of polymers by md simulations on small fragments in solution. application to cellulose. *The Journal of Physical Chemistry B*, 101(42):8454–8459, 1997.
- [89] Victor Rühle and Christoph Junghans. Hybrid approaches to coarse-graining using the votca package: liquid hexane. *Macromolecular Theory and Simulations*, 20(7):472–477, 2011.
- [90] Sikandar Yusufoddin Mashayak, Mara N Jochum, Konstantin Koschke, Narayana R Aluru, Victor Rühle, and Christoph Junghans. Relative entropy and optimization-driven coarse-graining methods in votca. *PLoS one*, 10(7):e0131754, 2015.
- [91] Fabian Grünewald, Riccardo Alessandri, Peter C Kroon, Luca Monticelli, Paulo CT Souza, and Siewert J Marrink. Polyply; a python suite for facilitating simulations of macromolecules and nanomaterials. *Nature communications*, 13(1):68, 2022.
- [92] Yoshihiko Ozaki, Yuki Tanigaki, Shuhei Watanabe, and Masaki Onishi. Multiobjective tree-structured parzen estimator for computationally expensive optimization problems. In *Proceedings of the 2020 genetic and evolutionary computation conference*, pages 533–541, 2020.
- [93] M Willjuice Iruthayarajan and S Baskar. Covariance matrix adaptation evolution strategy based design of centralized pid controller. *Expert systems with Applications*, 37(8):5775–5781, 2010.
- [94] Takuya Akiba, Shotaro Sano, Toshihiko Yanase, Takeru Ohta, and Masanori Koyama. Optuna: A next-generation hyperparameter optimization framework. In *Proceedings of the 25th ACM SIGKDD international conference on knowledge discovery & data mining*, pages 2623–2631, 2019.
- [95] Xiaodong Li, Wei-Che Chang, Yuh J Chao, Rizhi Wang, and Ming Chang. Nanoscale structural and mechanical characterization of a natural nanocomposite material: the shell of red abalone. *Nano Letters*, 4(4):613–617, 2004.

- [96] Bharath Natarajan and Jeffrey W Gilman. Bioinspired bouligand cellulose nanocrystal composites: a review of mechanical properties. *Philosophical Transactions of the Royal Society A: Mathematical, Physical and Engineering Sciences*, 376(2112):20170050, 2018.
- [97] Dennis C Glass, Kei Moritsugu, Xiaolin Cheng, and Jeremy C Smith. Reach coarse-grained simulation of a cellulose fiber. *Biomacromolecules*, 13(9):2634–2644, 2012.
- [98] Loukas Petridis, Hugh M O’Neill, Mariah Johnsen, Bingxin Fan, Roland Schulz, Eugene Mamontov, Janna Maranas, Paul Langan, and Jeremy C Smith. Hydration control of the mechanical and dynamical properties of cellulose. *Biomacromolecules*, 15(11):4152–4159, 2014.
- [99] YuanZhen Hou, Qing-Fang Guan, Jun Xia, Zhang-Chi Ling, ZeZhou He, Zi-Meng Han, Huai-Bin Yang, Ping Gu, YinBo Zhu, Shu-Hong Yu, et al. Strengthening and toughening hierarchical nanocellulose via humidity-mediated interface. *ACS nano*, 15(1):1310–1320, 2020.
- [100] Yuanyuan Guo, Wei Wang, and Xuewei Jiang. Molecular dynamics study on mechanical properties of cellulose with water molecules diffusion behavior at different oxygen concentrations. *Forests*, 14(2):371, 2023.

Supplementary Information

The following subsections and data are included in the Supplementary Information.

Force and energy curve of HB and LJ potentials
Sensitivity and ablation check for potential formula
All atom transverse stretch performance at different stretch speed
Temperature and pressure curve using 12 fs timestep
Component match degree of training loops
Bonded properties without rescale
Transverse strength and toughness distributions
Transverse stretch curves and distributions
Bonded geometry parameter distributions
Nonbonded equilibrium distance distributions
Additional structural properties
Baseline method structures for coarse grained models
Training using reward function without threshold
Training using other optimization methods
Secondary summits of the bonded geometry parameter distributions

Table S1, Table S2, Table S3, Table S4

Figure S1, Figure S2, Figure S3, Figure S4, Figure S5, Figure S6, Figure S7, Figure S8,
Figure S9, Figure S10, Figure S11, Figure S12, Figure S13, Figure S14, Figure S15,
Figure S16, Figure S17, Figure S18, Figure S19, Figure S20

Analytical coarse grained potential parameterization by Reinforcement Learning for anisotropic cellulose

Xu Dong^{1,*}

¹Department of Engineering Mechanics, Zhejiang University, Hangzhou 310027, China

Keywords: Reinforcement Learning, Boltzmann inversion, coarse grained, cellulose, anisotropy, hydrogen bonds

Supplementary Information

Force and energy curve of HB and LJ potentials

Defined with different Lennard-Jones style functions, the LJ potential we used applies an energy shift and force smoothing to ensure that both energy and force reach zero at the cutoff distance; the HB potential is influenced by the A:H-D angle. The force and energy curves of the HB and LJ potentials are shown in Figure S1, with $\epsilon = 1$ and $\sigma = 1$ in both cases.

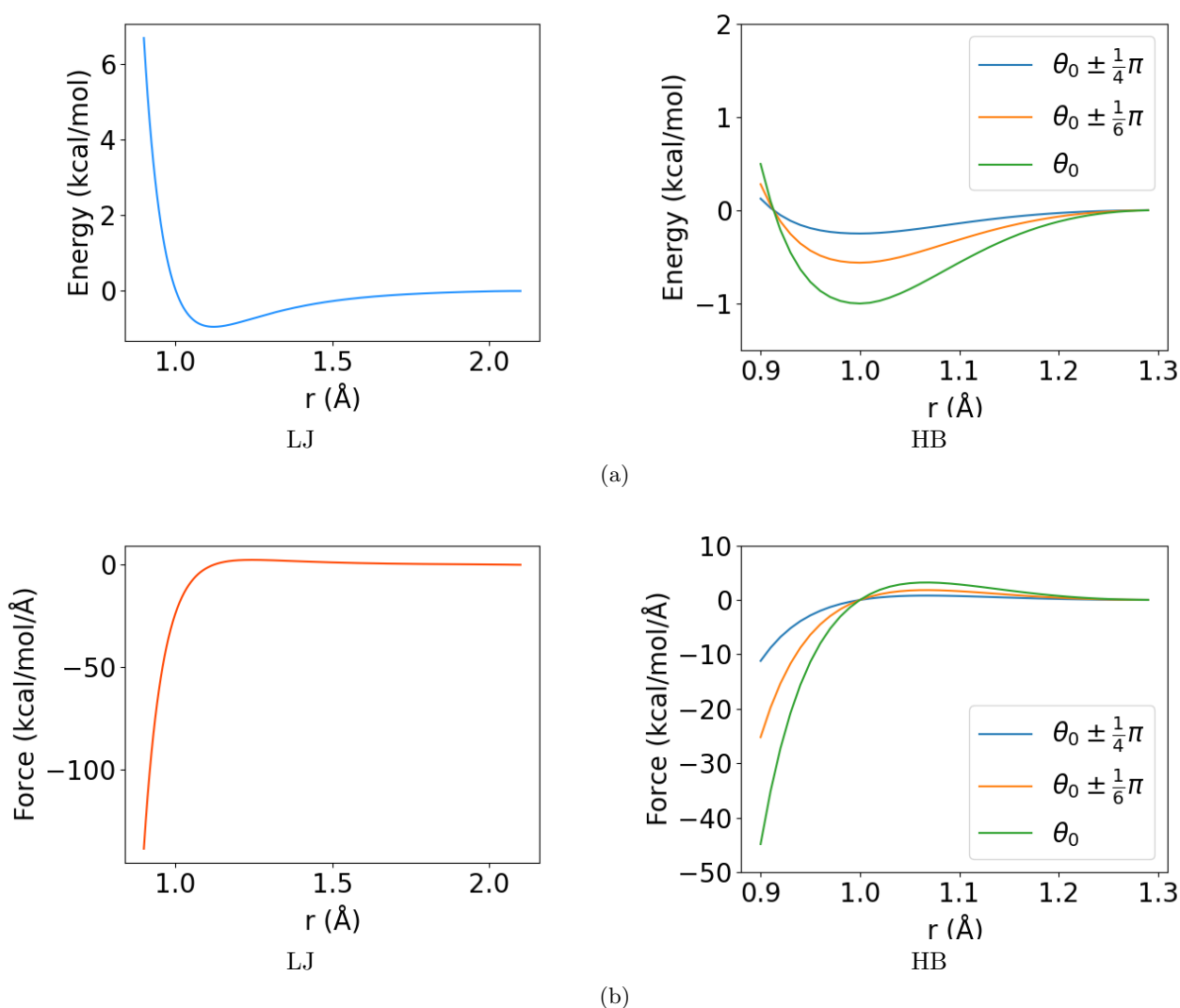


Figure S1: NB energy and force curves. (a) LJ and HB energy curves. (b) LJ and HB force curves. Both the LJ and HB potentials are based on Lennard-Jones interactions, and they follow the 12-6 and 12-10 formulas respectively. The key difference is that the HB potential is scaled by the power of the cosine of the A:H-D angle, while the energy shift and force smoothing of the LJ potential confirm zero energy and force at the cutoff distance. These curves are defined using $\epsilon = 1.0$ and $\sigma = 1.0$. More specifically, $r_{in} = 2.0$ and $r_{cut} = 2.1$ for the LJ potential, and $r_{in} = 2.0$ and $r_{cut} = 2.1$ for the HB potential.

*Corresponding author, Email: donx@zuaa.zju.edu.cn

Sensitivity and ablation check for potential formula

The choosing of Lennard-Jones potential in this model was lack of strong physics background. The main reason for LJ potential was the simplicity and easiness to stabilize geometry structure based its stationary point. The cut, smoothing, and directionality were also artifacts. Sensitivity and ablation check for the potential forms are necessary thereby. Based on the optimized coefficients mentioned in the main paper and lock all the bonded potential coefficients, half/double energy coefficients σ half/double energy coefficients (while distance coefficients were kept), 0.8/1.2 times distance coefficients (while energy coefficients were kept) were tested with 100 replica simulations. Besides, although we just followed the original paper and used fourth power for cosine in the formula, second, sixth, and eighth power were also tested (while all other coefficients were kept). All the data for sensitivity and ablation were listed in Table S1 and Table S2. These data elucidated that the potential function form we used were not significantly sensitive to coefficients, the results for obviously deviated coefficients were quantitative rather than qualitative or crashing.

Table S1: Sensitivity and ablation check equilibrium thermodynamics

	type	Temperature (T)	Pressure YY (MPa)
ϵ	0.5x	300.2±0.1	18.4±0.7
	2.0x	300.3±0.1	13.4±0.8
σ	0.8x	300.2±0.1	86.0±1.2
	1.2x	300.7±0.1	-4.2±0.5
\cos^n	2	300.2±0.1	6.2±0.7
	6	300.3±0.1	10.0±0.8
	8	300.2±0.1	2.5±0.8
θ_0	180.0	300.0±0.1	25.1±0.7
HB	no	300.0±0.1	-13.6±0.7
	CG	300.2±0.1	11.9±0.7
	AA	299.9±0.0	-0.8±1.2

Table S2: Sensitivity and ablation check nonbonded properties

type	Strength (MPa)			Toughness (GPa)			
	V	H	S	V	H	S	
ϵ	0.5x	522.0±4.8	252.0±0.7	223.6±3.0	53.3±1.5	38.5±0.7	70.7±2.1
	2.0x	2550.2±6.2	1520.0±4.4	1165.9±9.7	228.6±5.6	406.4±7.7	347.5±8.1
σ	0.8x	447.2±9.5	30.6±0.7	387.8±4.9	89.1±3.3	1.3±0.2	146.2±5.6
	1.2x	654.8±21.5	568.6±14.7	500.1±10.9	100.0±3.3	116.1±3.3	155.3±5.6
\cos^n	2	1244.1±4.7	617.0±0.9	498.3±4.7	123.5±3.1	109.8±3.7	164.5±4.2
	6	1177.8±7.3	672.7±1.1	512.7±4.0	111.7±2.9	77.2±0.5	159.9±4.0
	8	1178.5±6.9	686.5±1.0	511.7±5.2	121.2±3.4	77.6±0.4	155.5±4.1
θ_0	180.0	1168.9±7.5	637.4±1.0	506.7±4.2	112.6±3.1	84.7±2.0	151.2±4.0
HB	no	718.7±4.6	520.4±2.0	357.3±2.8	98.7±3.1	141.5±1.5	98.7±3.4
	CG	1191.9±6.0	653.5±1.1	509.8±4.6	117.0±3.2	78.1±1.2	166.9±3.8
	AA	1224.0±9.7	638.2±4.2	467.0±3.7	111.0±2.5	77.9±2.8	190.1±4.6
Error							
ϵ	0.5x	57%	61%	52%	52%	51%	63%
	2.0x	108%	38%	150%	106%	422%	83%
σ	0.8x	63%	95%	17%	20%	98%	23%
	1.2x	47%	11%	7%	10%	49%	18%
\cos^n	2	2%	3%	7%	11%	41%	13%
	6	4%	5%	10%	7%	1%	16%
	8	4%	8%	10%	9%	0%	18%
θ_0	180.0	5%	0%	9%	1%	9%	20%
HB	no	41%	18%	23%	11%	82%	48%
	CG	3%	2%	9%	5%	0%	12.2%

All atom transverse stretch performance at different stretch speed

For the slant models, frictional sliding was quantitatively determined by the direction angle, which was defined as the projection angle of the edge carbon atoms on the ring (Figure S5). Before choosing 10.0 nm/ns as the stretch speed for

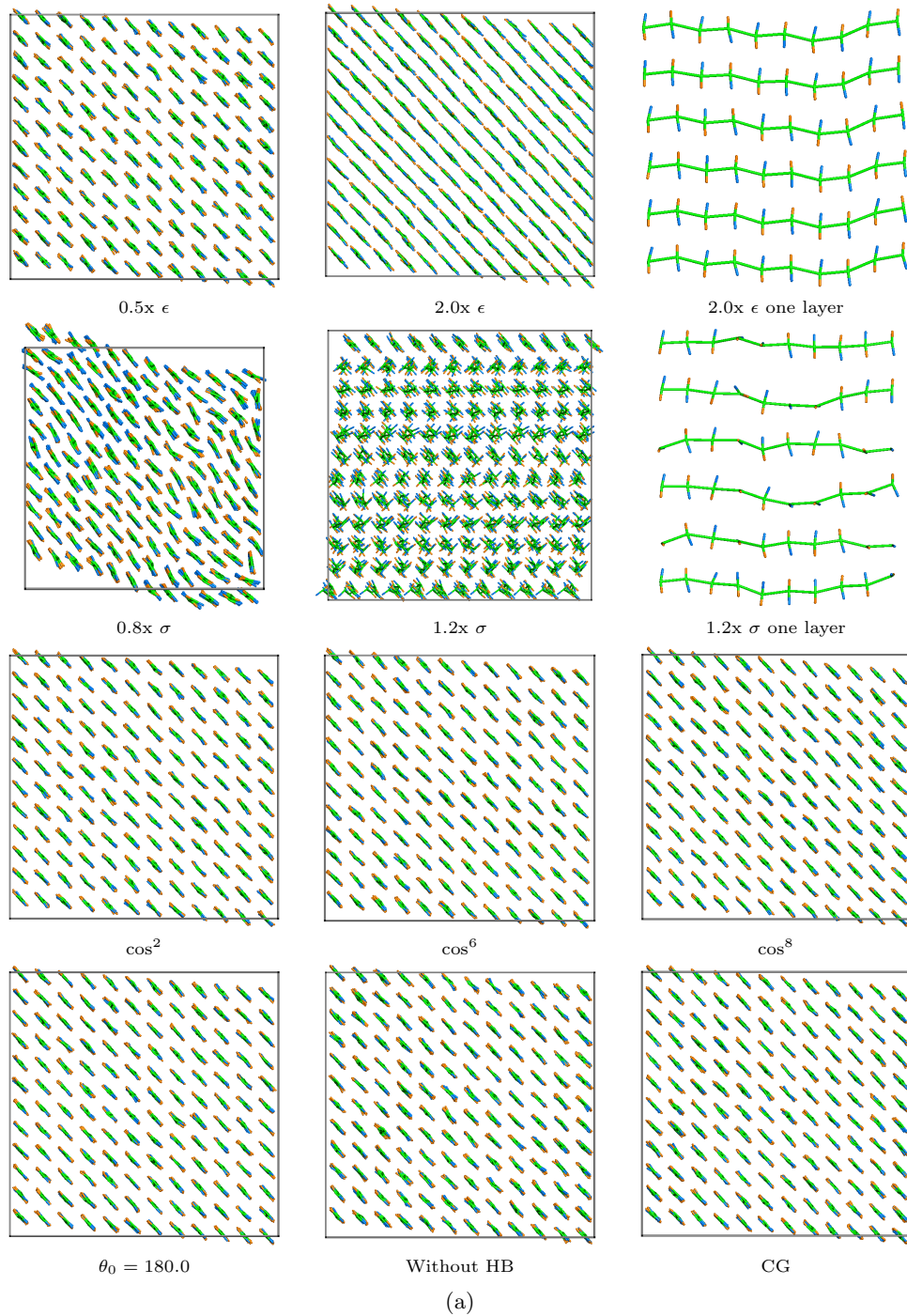


Figure S2: Sensitivity and ablation check relaxation structures. The rationality of Lenard-Jones potential application in the CG level need sensitivity and ablation check. For the sensitivity check, NB energy coefficients ϵ were scaled to be half or double; NB distance coefficients σ were scaled to be 0.8 times less or 1.2 times more; the power of cosine of HB potential was changed to 2, 6, 8 instead of 4. For the ablation check, θ_0 in the HB potential was reset to π or the HB potential was fully removed. For all of these options and the unchanged reference (marked as CG, using the same coefficients in the paper), the structures after relaxation/before stretch were all provided. Relaxation structures demonstrated the robustness of NB potential function forms, but large energy coefficients or unmatched distance coefficients caused unstable structures, as the one layer figure showed.

potential parameterization, the transverse stretch performance data in the three characteristic directions at 0.1, 1.0, 2.0, 4.0, 10.0, 20.0 and 40.0 nm/ns are checked (Figure S3). Except for 0.1 nm/ns (at which speed 10 replica simulations are executed to save resources), 100 replica transverse stretch performance data were collected. These results confirm that the stretch speed is not a critical factor for the transverse stretch performance data, and the performance deviations at other speeds are nearly all less than 15% based on the average data at 10.0 nm/ns. Only the toughness data of the vertical model at 40.0 nm/ns was beyond 15% and 10.0 nm/ns was chosen. Stress-strain curves with maximum stress distribution and strain energy curves with maximum strain energy distribution at 10.0 nm/ns are also provided in Figure S4.

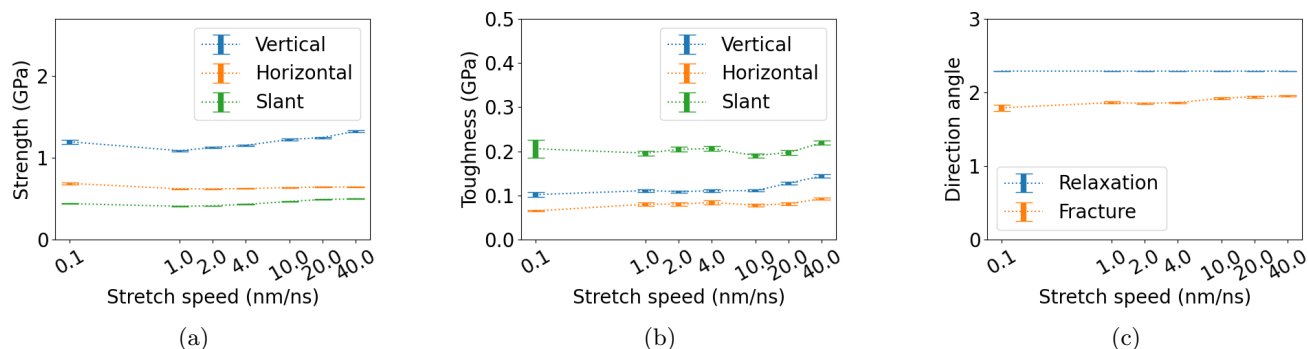


Figure S3: AA transverse stretch performance with respect to speed. Transverse (a) strength, (b) toughness and (c) direction angle with standard errors at different stretch speeds are presented. 100 replica transverse stretches at stretch speeds of 1.0, 2.0, 4.0, 10.0, 20.0 and 40.0 nm/ns were summarized with averages and standard errors. Only 10 replica at 0.1 nm/ns were enforced to control computation costs. All data except for toughness of vertical models at 40.0 nm/ns were within 15% relative deviations referenced to average values at 10.0 nm/ns. 10.0 nm/ns was chosen for parameterization finally.

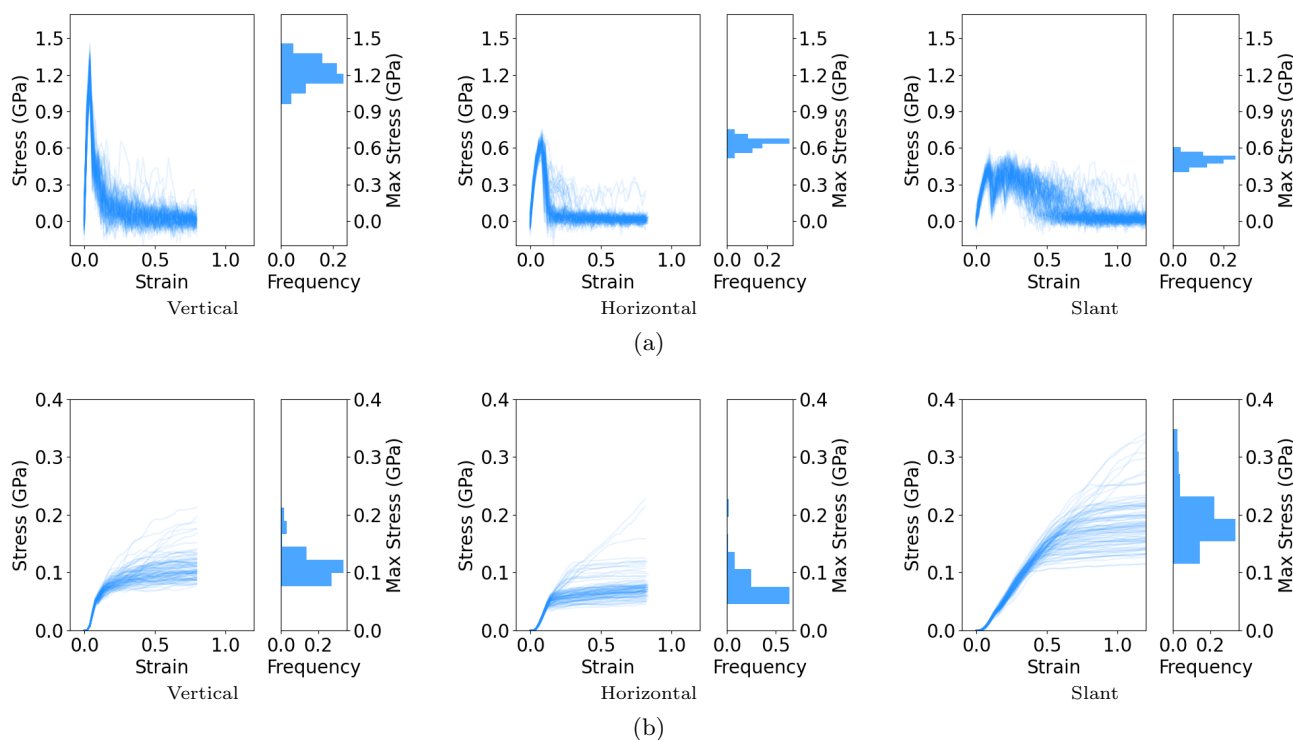


Figure S4: AA stretch curve collections. (a) Stress-strain and (b) strain energy collection of AA transverse stretches in characteristic directions at 10.0 nm/ns. Each collection contains 100 curves, and the strength or toughness distribution is enclosed on the right.

Temperature and pressure curve using 12 fs timestep

The size of timestep is one critical quantity for the coarse grained models. A small timestep could ensures system stability but sacrifices computation efficiency. For the simulations for axial stretch and polymer stiffness, a small 4 fs was chosen; for the more expensive simulations for transverse stretch, a larger 12 fs was chosen. 12 fs timestep was a direct bisection result of 10 fs and 15 fs to ensure system stability. To confirm the suitability of this 12 fs timestep, an equilibrium state simulation without any external loads was performed by a CNC slant model under NPT ensemble (as the same for transverse stretch) for both AA and CG. The timestep used for AA was 2 fs. The temperature and pressure in the vertical

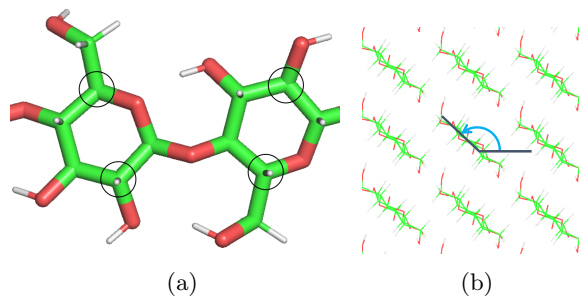


Figure S5: Definition of direction angle. (a) Carbon atoms considered for the direction angle. (b) The projection angle of the considered carbon atoms is defined as the direction angle for the AA models, whereas the CL1 and CL2 beads are used for the CG models. The direction angle was defined to quantify the frictional sliding of the slant models.

direction (Pressure YY) was illustrated in Figure S6. As the figures shown, the amplitude for temperature and pressure of CG model was slightly larger but also stable.

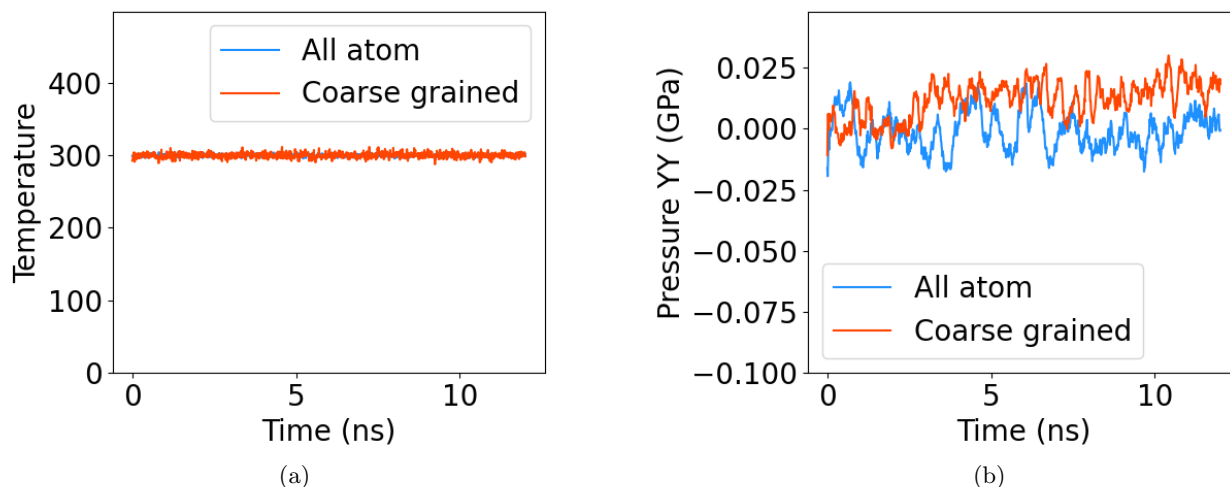


Figure S6: (a) Temperature and (b) pressure curves from the 12 ns slant model equilibrium state simulations using timestep 2 fs for AA and 12 fs for CG. The comparison between all atom and coarse grained models confirmed the suitability of timestep and stability of thermodynamics. Comparing to the all atom, the coarse grained model with much higher timestep was also stable in the context of deviation, but the deviation were acceptably larger.

Component match degree of training loops

The reward function for RL training was composed of match degrees, and their thresholds and weights. To describe the learning process during training, component match degrees curves with training steps in both the first training loop and the last training loop were provided in the Figure S7. As included in the table of bonded and nonbonded properties, the component match degrees were of elastic modulus, persistence length, end to end distance, transverse strength, and toughness. The match degree of persistence length or end to end distance was the minimal value of three chain lengths (10, 20, 30 residues long); the match degree of transverse strength or toughness was the minimal value of three characteristic directions.

For echo marked column, the upper one was from the first training loop while the lower one was from the last training loop. As the figures shown, the axial modulus was well matched even at the very beginning; and the transverse mechanical properties were obviously improved after training.

So the only problem was about polymer stiffness, it seemed that no evidence for obvious improvement. That was not the problem of computation convergence, as 4 fs timestep was chose and the polymer stiffness value stability was tested by extending simulations steps as 4 times longer. As emphasized in the bonded properties, rescaling of angle and dihedral force constants was critical to compensate lower degrees of freedom while keeping polymer stiffness. It confirmed the difficulty to quantitatively reproduce polymer stiffness in the CG model. Thus, the optimization of polymer stiffness was actually a selection process. To harden the validation for all the three chain lengths, thus three different chain lengths were all considered in the training. And the match degree function for polymer stiffness was slightly different:

$$m = \frac{1}{1 + \sqrt{\left| \frac{y_1 - y_0}{y_0} \right|}} \quad (\text{S1})$$

The square root function will further lowering the match degree for low match degree.

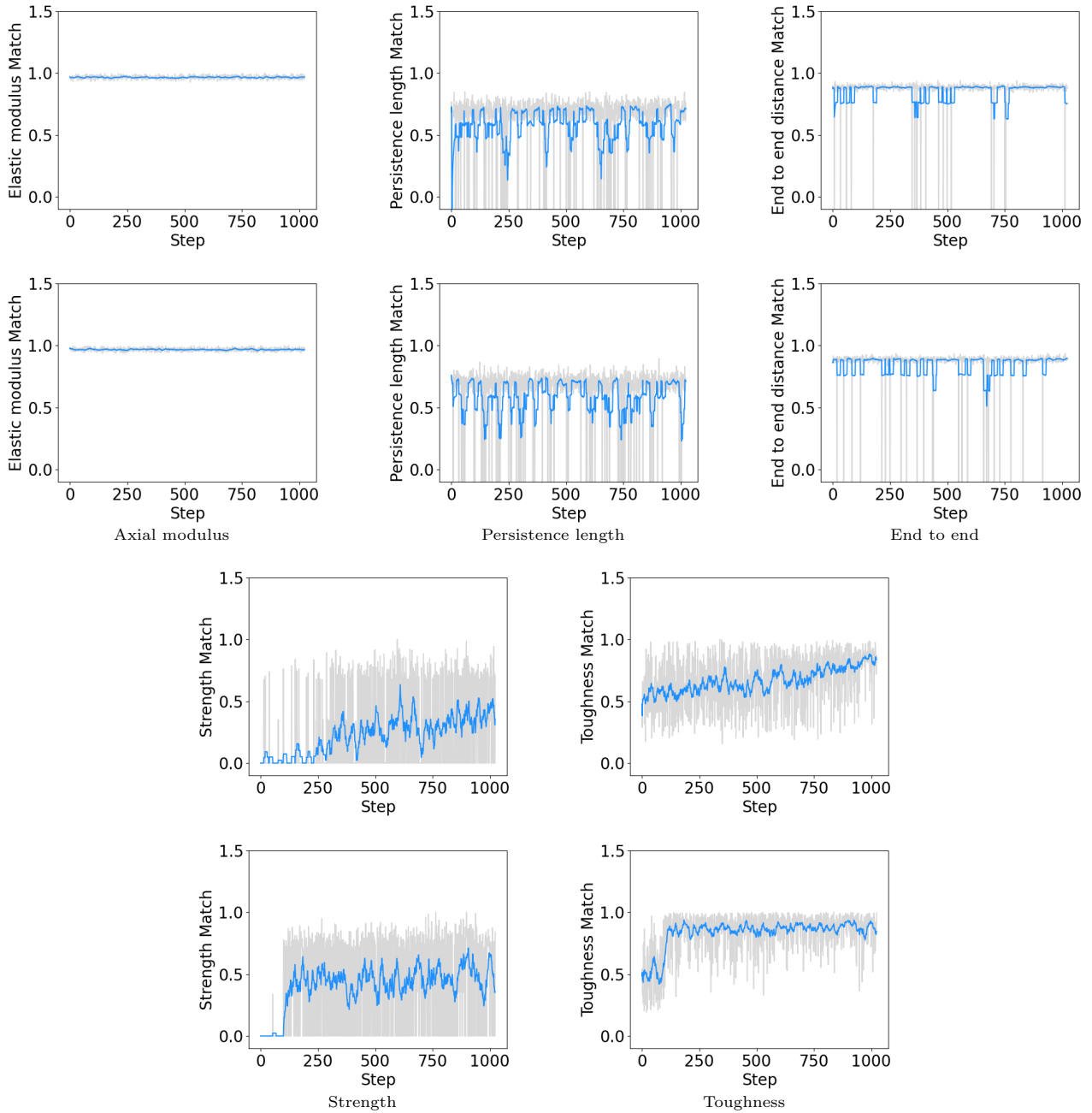


Figure S7: Component match degrees of reward function in the first (upper) and last (lower) training loop. The match degrees of transverse strength and toughness confirmed the optimization by RL. For the axial modulus and polymer stiffness, the optimization was selection in fact. Thus, polymer stiffness of three chain lengths were all computed to ensure the validation together with a specific strict match degree function.

Bonded properties without rescale

In this study, the BD force constants were rescaled to smaller values, referring to the estimations using the Boltzmann inversion method (Table S3). The BD properties corresponding to the unrescaled BD force constants are listed in Table S4, where the persistence length data are unacceptable. The degrees of freedom of the CG models are significantly smaller than those of their AA models, and we assume that the smaller BD force constants for the angles and dihedrals are critical for reproducing polymer stiffness performance.

Table S3: Bonded force constants without rescale

type	id	Optimized	Unrescaled
$k(\text{kcal/mol}/\text{\AA}^2)$			
bond	1	64.06	110.3
	2	82.42	141.9
	3	112.3	193.3
$k(\text{kcal/mol})$			
angle	1	30.97	274.5
	2	38.79	343.7
	3	30.52	270.5
	4	27.28	241.8
	5	25.97	230.2
	6	22.42	198.7
$k(\text{kcal/mol})$			
improper	1	0.1702	21.57
	2	0.1555	19.71
	3	0.1698	21.53

Table S4: Bonded properties without rescale

type		AA	CG	Error
Axial modulus (GPa)		133.5	233.8	75.13%
Persistence length (nm)	10	9.755	306.1	3137.87%
	20	9.815	310.5	3063.53%
	30	9.716	298.6	2973.33%
End-to-end distance (nm)	10	4.523	4.689	3.67%
	20	9.355	9.888	5.70%
	30	13.536	15.069	11.33%

Transverse strength and toughness distributions

The NB properties include the transverse strength and toughness, as shown in Figure S8. Although the accuracy of strength and toughness distributions is problematic owing to the representability problem of CG models, the full distributions of transverse strength and toughness are shown in Figure S8 for reference.

Transverse stretch curves and distributions

Transverse stretch curves and distributions of 100 replica simulations are provided to elucidate the reproduced transverse anisotropy (Figure S9). The direction angle of the slant model is also shown to describe frictional sliding. These results confirmed that, the fragility of the vertical and horizontal models and the toughness of the slant models are all represented in the CG model. Two stress summits were observed in the stress-strain curves of the vertical model, which were caused by the horizontal dislocations. When the HBonding layers broke in the vertical models, these layers rotated and reconnected, resulting in two fractures and two stress summits.

Bonded geometry parameter distributions

After parameterization, the bonded geometry parameters were sampled from the CNC equilibrium and stretch trajectories using the CG model and the mapped AA trajectories (Figure S10, Figure S11). The bonded geometry parameters of the

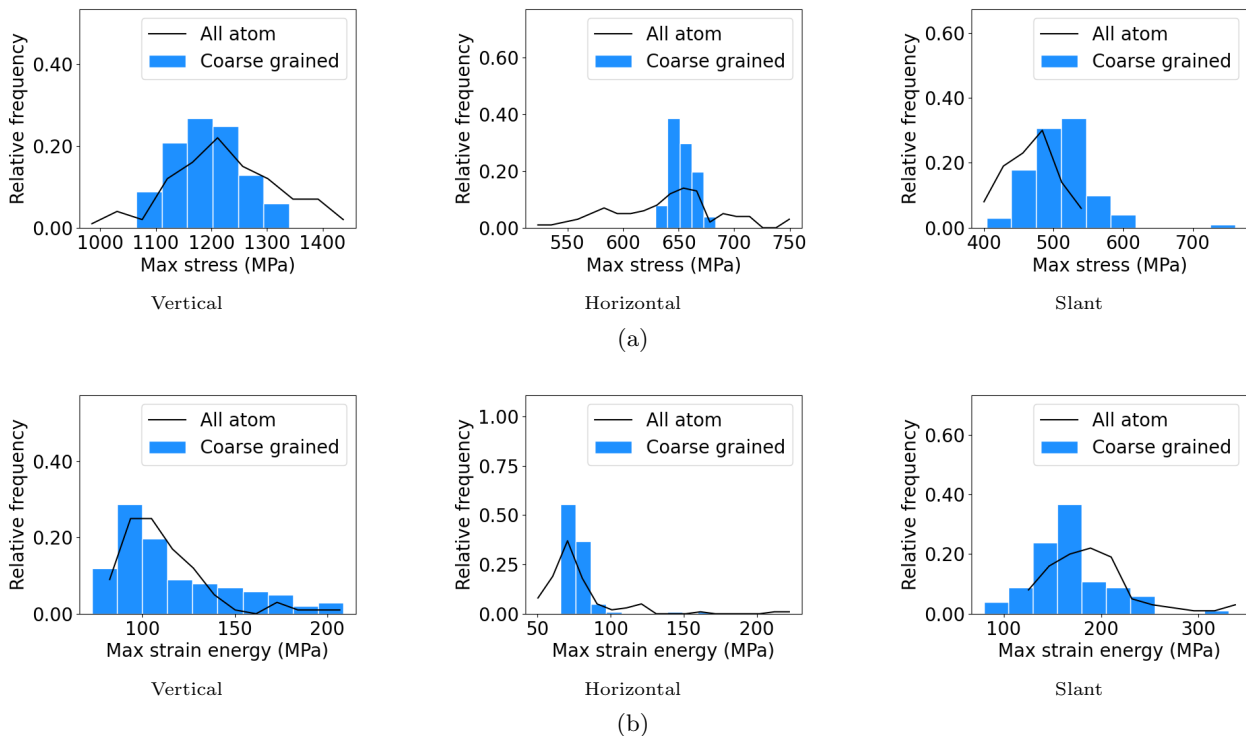


Figure S8: Transverse (a) strength and (b) toughness distributions. A total of 100 replica simulations were performed with different random seeds for both AA and CG models in three directions. For the vertical and slant models, the strength and toughness histograms were reproduced consistently, because their mean values and standard errors were similar. Despite the accuracy of the mean values, the horizontal CG models provided narrower distributions, which was within expectations.

CG models were similar to those of the AA reference data. However, the distributions of the CG models exhibited larger dispersions caused by the rescaled BD force constants.

Nonbonded equilibrium distance distributions

After parameterization, nonbonded equilibrium distances were sampled from the CNC equilibrium and stretch trajectories using the CG model and the mapped AA trajectories, as shown in Figure S12 and Figure S13. As mentioned in the Results-Coefficients section, NB distance coefficients are usually larger than the estimated range $[0.89d^e, 1.00d^e]$ after parameterization by RL. However, the equilibrium distance of the CL2:CL3 pair was not significantly larger, which emphasized the complexity of this coarse grained model and demonstrated the increase in σ_{p23} . The errors in the equilibrium distance distributions are acceptable and less than 15%.

Additional structural properties

The radical distribution function, radius of gyration, and root-mean-square deviation of the slant CNC equilibrium trajectories obtained using the CG models were compared with those of the mapped AA trajectories (Figure S14). These results demonstrate the effectiveness of the CG model.

Baseline method structures for coarse grained models

Except for the RL parameterized CG potential, baselines models were also tested in parallel. The simulations we used for AA and CG baselines were the slant model equilibrium without any external loads under NPT ensemble as we used for the RL parameterized model. The reference AA trajectory was simulated for 20 ns with timestep 2 fs.

Bottom-up baselines included IBI, RE, and FM and Top-down baseline MARTINI 3 were compared to illustrate the necessity of this hybrid-hybrid model. Except for the numerical properties in the tables, structures after relaxation and fracture are illustrated in the Figure S15 and Figure S16. Owing to its weak NB interactions and high fracture strain and toughness, fracture structures shown for MARTINI in the horizontal and slant characteristic directions was not fractured yet because it WAS stripped like a ribbon before fracture. The resultant results of these bottom-up baselines confirm the validation and superiority of this RL parameterized model following extended bottom-up approach.

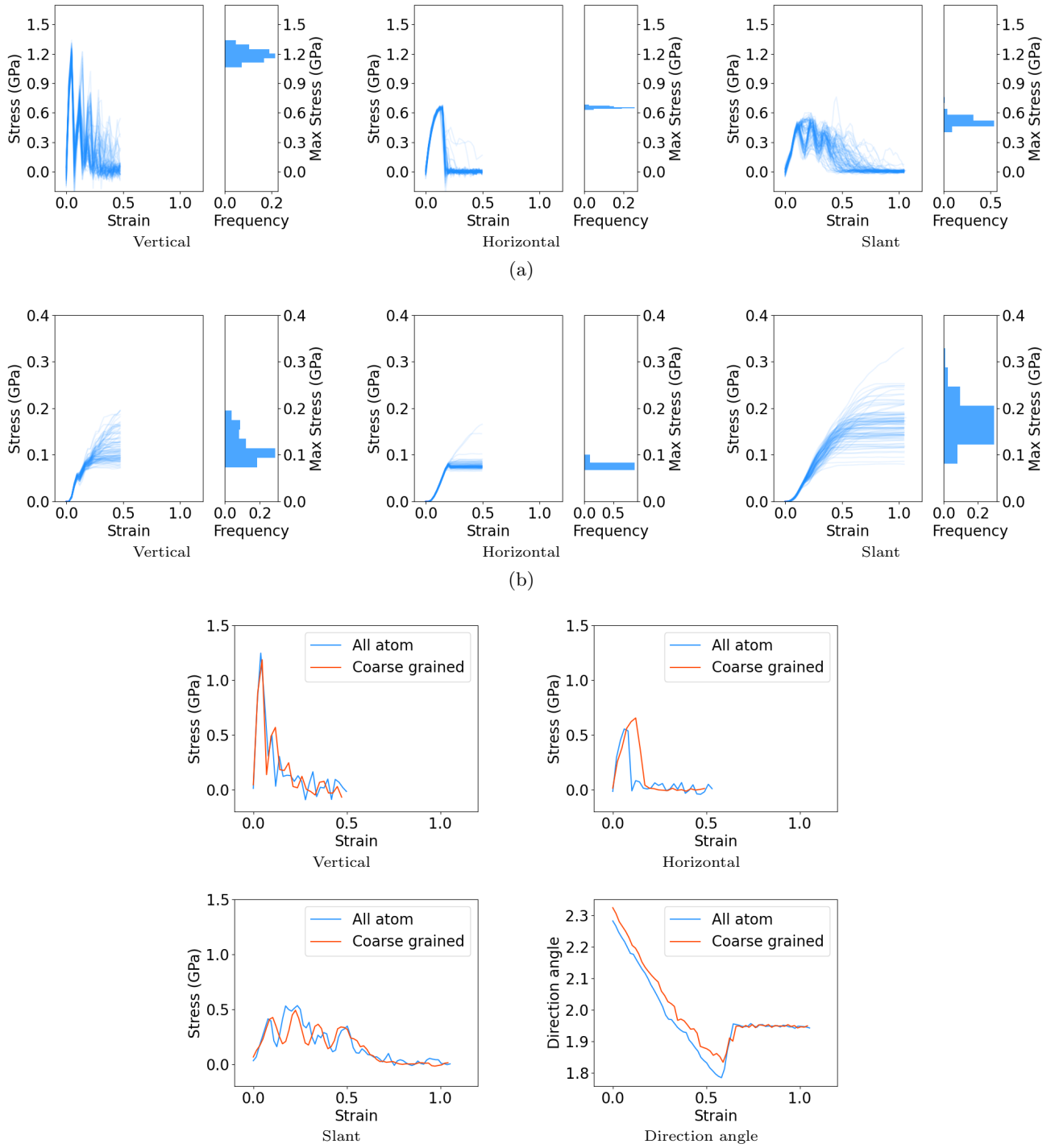


Figure S9: CG stretch curve collections. CG transverse stretch (a) stress-strain and (b) strain energy collections in characteristic directions at 10.0 nm/ns. Each collection contains 100 curves, and the strength or toughness distribution is enclosed on the right. The two summits of the stress-strain curves for the vertical models were caused by horizontal dislocations. This implied that the fractured HBonding layers rotated and reconnected to their nearby layers and broke again. (c) Examples of transverse stress-strain curves in the characteristic directions. An example of the direction angle of the slant model is also included to quantitatively describe the frictional sliding. The fragility and ductility of the different models are validated by the example curves.

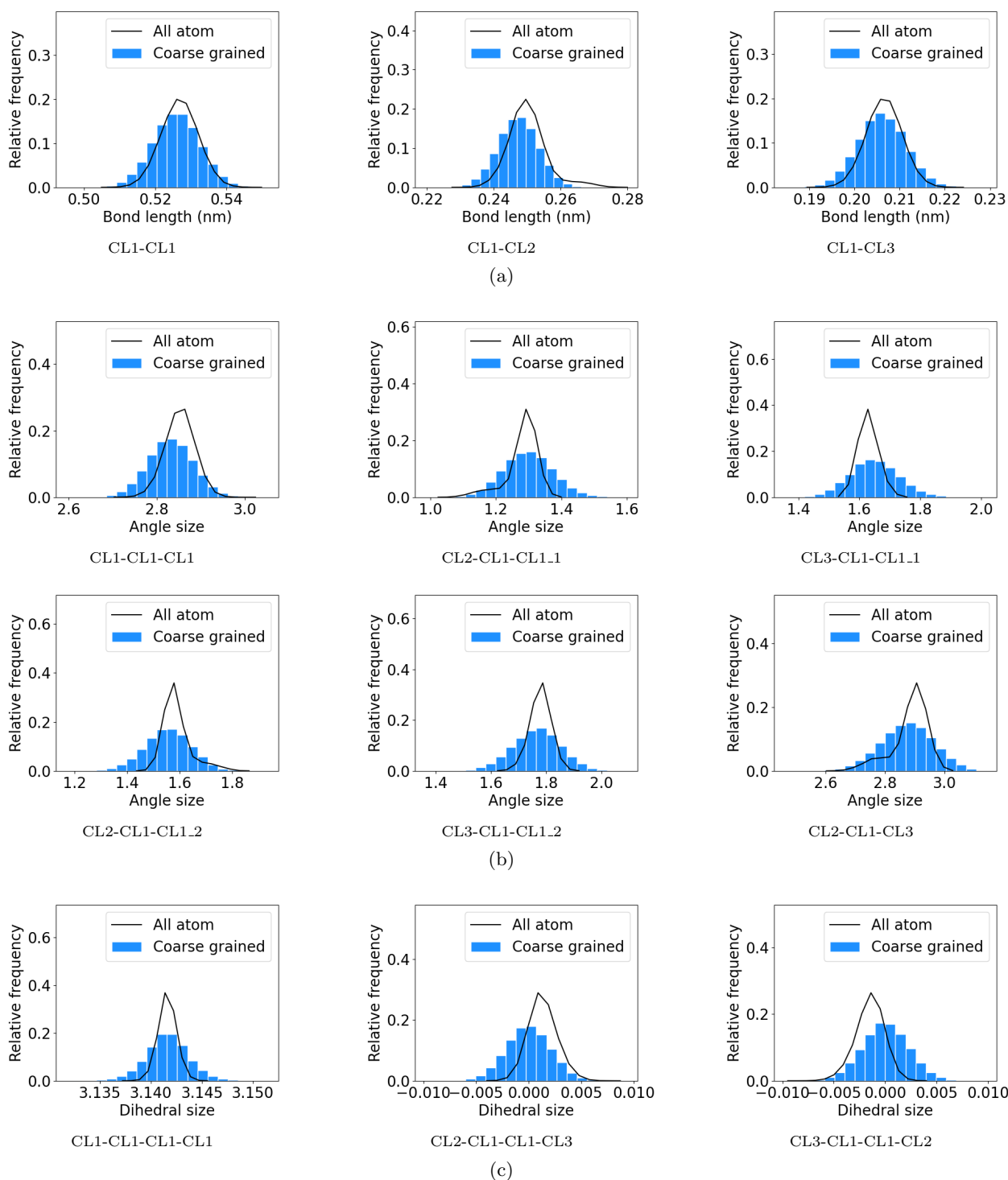


Figure S10: Bonded geometry parameter distributions of equilibrium states. Distributions of (a) bond length, (b) angle size, and (c) dihedral size. These data were derived from the equilibrium CNC trajectories of the CG models and mapped AA trajectories. The bonded geometry parameters were well preserved in the CG model (with errors of less than 2%). Owing to the smaller force constants, the distribution dispersions were larger than those of the AA reference as a compromise for reproducing the polymer stiffness.

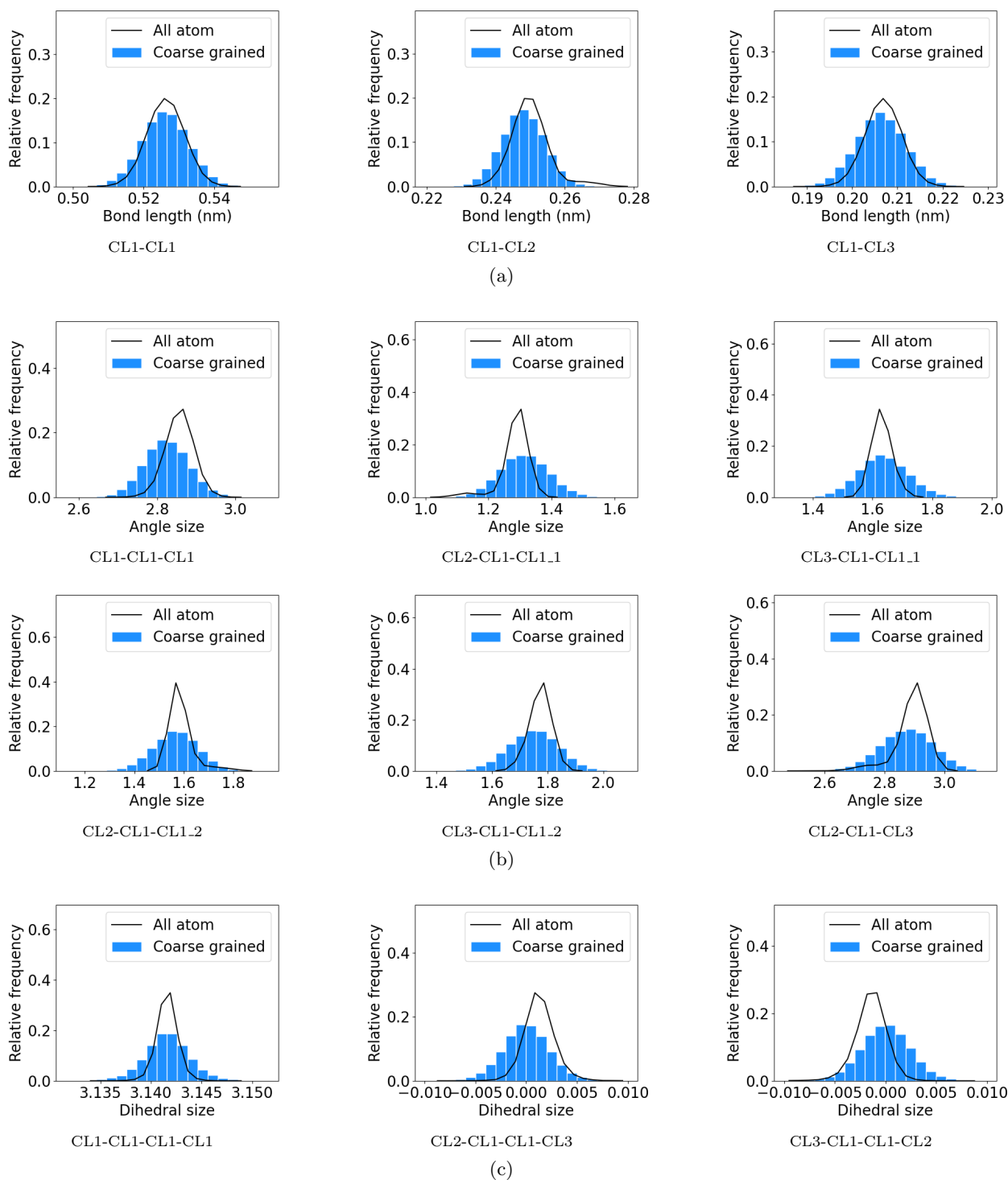


Figure S11: Bonded geometry parameter distributions of stretch states. Distributions of (a) bond length, (b) angle size, and (c) dihedral size. These data were derived from the stretch CNC trajectories of the CG models and mapped AA trajectories. The distributions of both AA and CG were quite close to the equilibrium data.

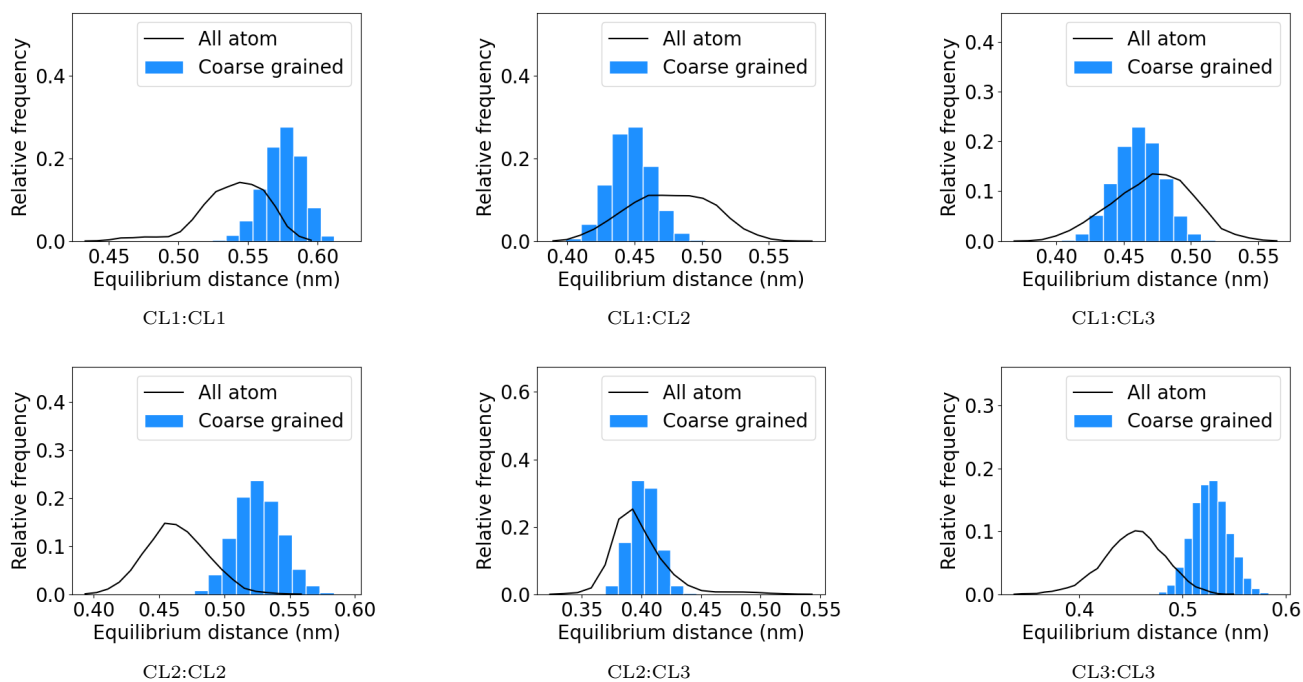


Figure S12: Nnonbonded equilibrium distance distributions of equilibrium states. These data were derived from the equilibrium CNC trajectories of the CG models and mapped AA trajectories. Corresponding to the unexpectedly larger NB distance coefficients, the equilibrium distances were often larger than those of the baselines to an acceptable extent with errors of less than 15%). However, the resultant equilibrium distances of CL2:CL3 were not larger than those of the AA reference data, which elucidates the complexity of the multiple particle models and aids in understanding the increase in σ_{p23} .

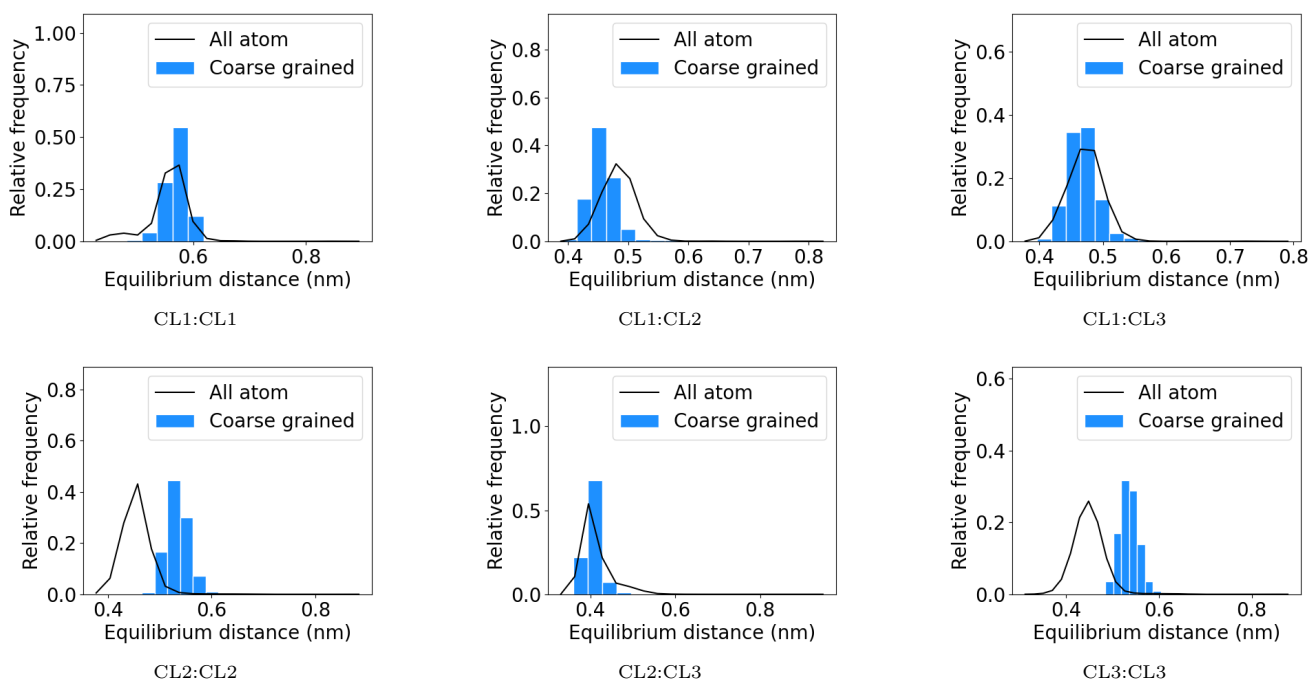


Figure S13: Nnonbonded equilibrium distance distributions of stretch states. These data were derived from the stretch CNC trajectories of the CG models and mapped AA trajectories. The distributions of both AA and CG were quite close to the equilibrium data.

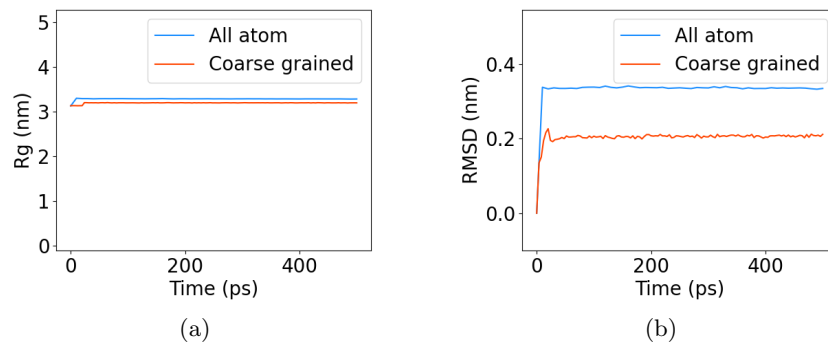


Figure S14: Additional structural properties. (a) Radius of gyration. (b) Root-mean-square deviation. These data were derived from the equilibrium CNC trajectories of the CG models and mapped AA trajectories. They provided additional information to demonstrate the structural similarities between CG and AA models.

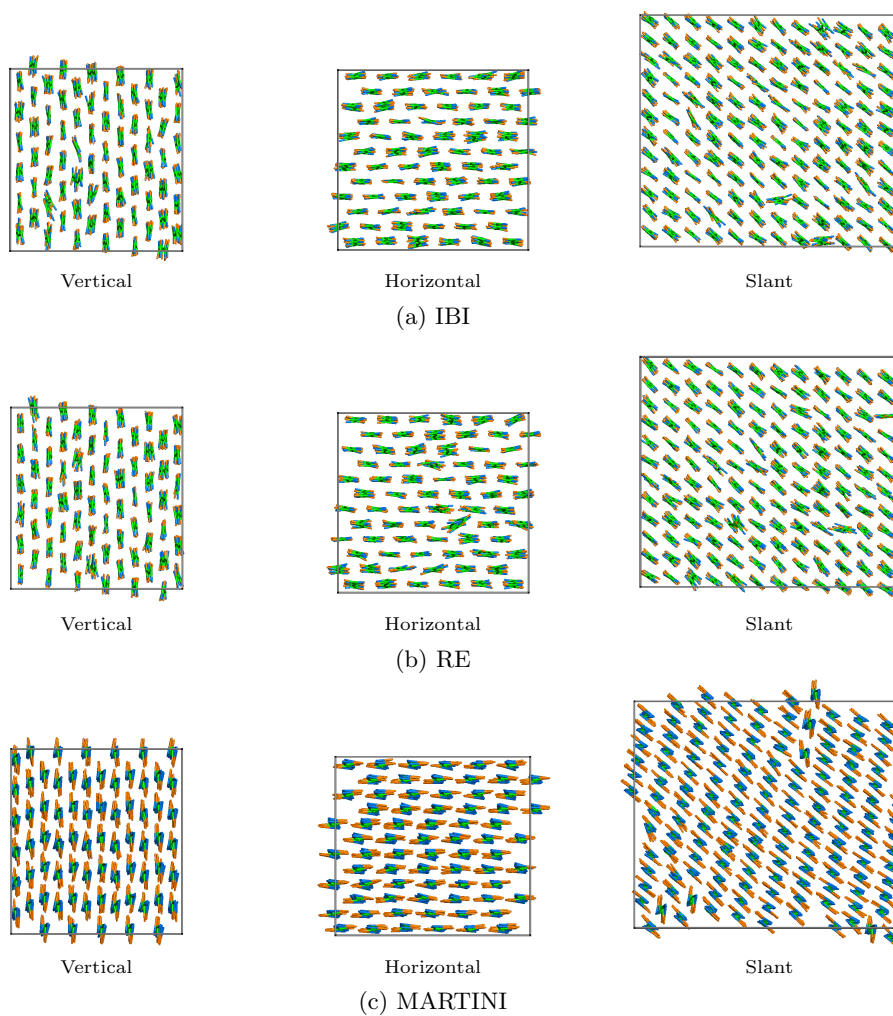


Figure S15: Baselines relaxation structures of CNC models by (a) IBI, (b) RE, and (c) MARTINI in characteristic directions. The models by IBI and RE were simulated under NVT ensemble without velocity generalization, and only MARTINI models were controlled by NPT ensemble. Even though, the mode by IBI and RE could not preserve laminar structures well as the MARTINI model did.

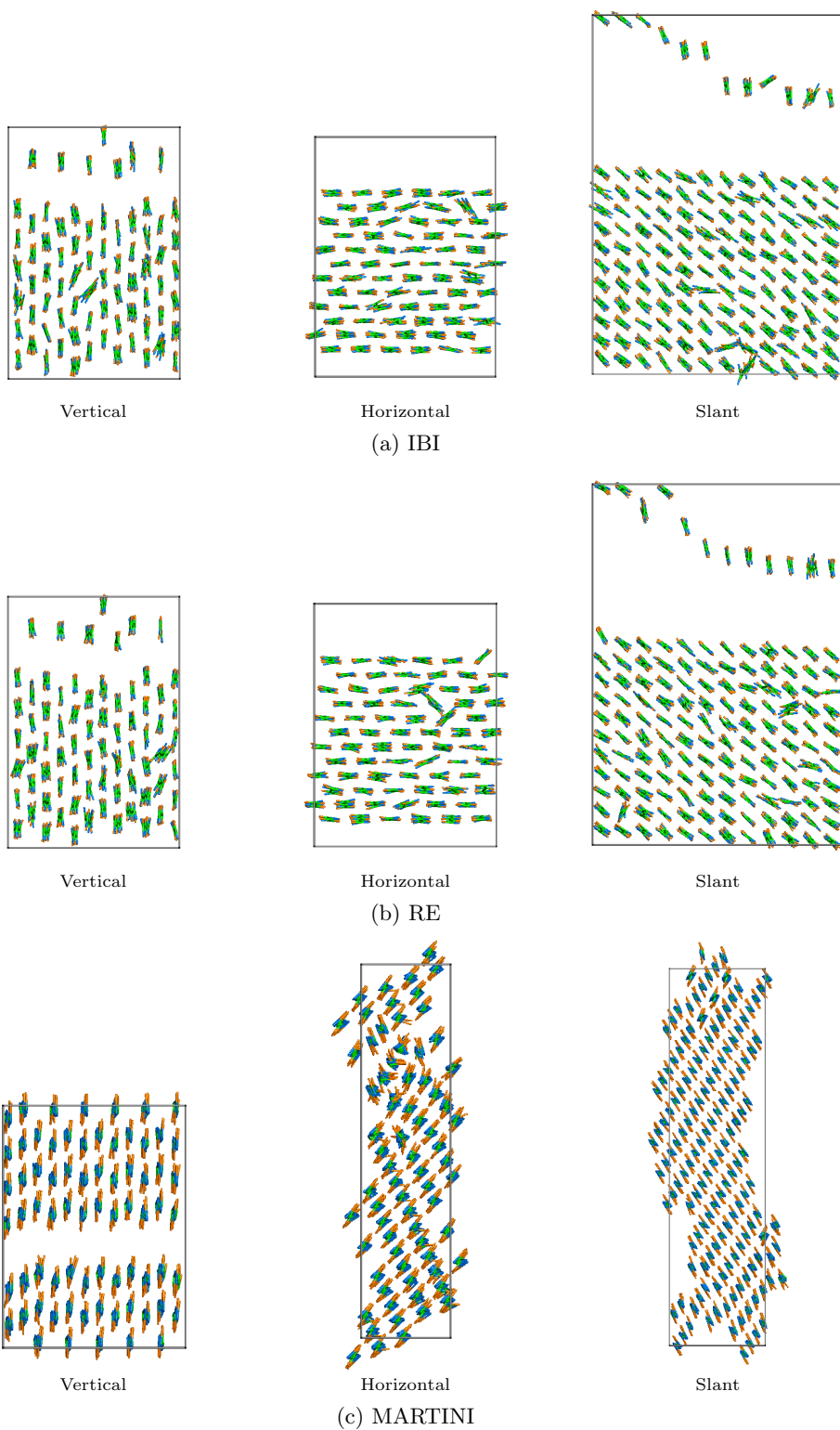


Figure S16: Baseline fracture behaviors of CNC models by (a) IBI, (b) RE, and (c) MARTINI in characteristic directions. The models by IBI and RE were simulated under NVT ensemble without velocity generalization, and only MARTINI models were controlled by NPT ensemble. Even though, the mode by IBI and RE could not reproduce the friction sliding behavior in the slant directions. The stretch result in the horizontal direction also emphasized the weak NB interactions of MARTINI 3 cellulose potential. The figures of MARTINI 3 in horizontal and slant directions were not even fractures, because their models were stretched to a long, thin strip and broke.

Training using reward function without threshold

As we mentioned in the paper, reward function was defined as a sum of match degrees. However, threshold was introduced to increase discrimination, and when considering the match degree of strength and toughness, minimal values was finally considered. Here, we made a parallel training using reward function without threshold and minimal cut to better elucidate the importance and robustness of thresholds:

$$M = \frac{1}{1 + \left| \frac{y_1 - y_0}{y_0} \right|} \quad (\text{S2})$$

. where y_0 and y_1 are the reference and sampled values, respectively. The reward function is the sum of a series of matching degrees, except for the transverse strength M_s and toughness M_t ,

$$\text{reward} = \sum M_i + w \cdot \frac{M_s + M_t}{2} \quad (\text{S3})$$

Anything else was the same as the training in the paper. The training convergence and component match degrees are provided 1, in the Figure S17 and Figure S18. It is obvious that training without threshold had higher average reward, but the critical maximum reward values are very close. As shown by the component match degrees, the slightly higher max reward is mainly a result of reward function form: it replaced $\min(M_s, M_t)$ with $\frac{1}{2}(M_s + M_t)$. These data confirmed the robustness of threshold first.

The real advantage of the reward function with threshold was emphasized by the higher chance to hit coefficients with high rewards, especially during the early training. This could be illustrated by the 20 maximum reward case for the first training loop (1024 training steps) using reward function with and without thresholds (Figure S17).

If we further concentrate on on the starting 200 steps and target at the step whose reward was higher than 80, we will notice something more important: When with threshold, although average reward was definitely lower, but it could hit good performance coefficients faster. This is really helpful especially during the early debug and development stage.

In conclusion, thresholds are not harmful for the training in the long time but hit good results faster at the beginning stage.

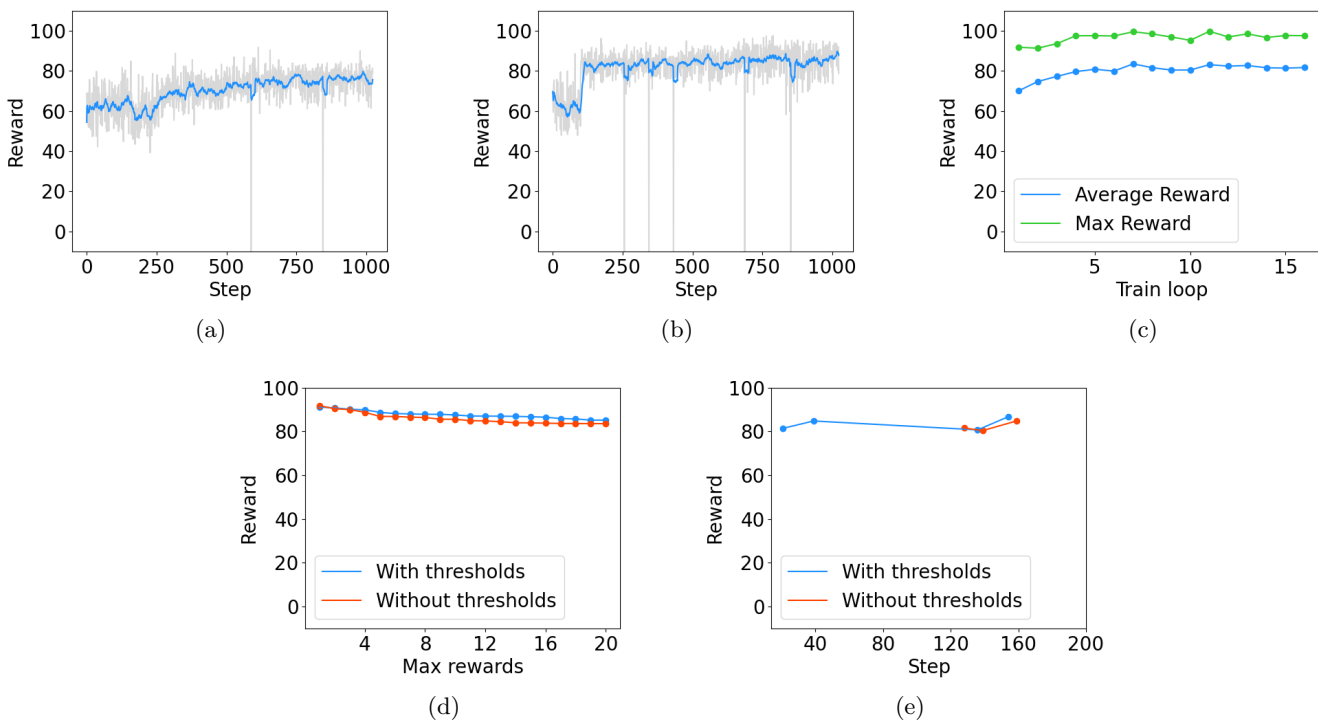


Figure S17: Training convergence and statistics without thresholds. (a) Reward and its moving average in the first and (b) last training loops. Each training loop contained 1024 training steps. The subsequent training loops with higher and more stable rewards were based on the former training loops. (c) Average and maximum rewards for different training loops. The average and maximum rewards confirmed the convergence. (d) Maximum 20 rewards in the first training loop from both with and without thresholds. (e) Rewards higher than 80.0 with steps in the 200 steps of first training loop from both with and without thresholds. These data were from parallel training which only changed reward functions without thresholds. The max rewards of training loops without thresholds were only slightly higher owing to the removal of minimal for M_s and M_t , this confirmed the robustness of thresholds. Besides, the maximum 20 rewards and the high rewards from the starting 200 steps further proved the advantages of thresholds: hitting coefficients with high rewards faster during early training. This was not critical but really helpful during the early development stage.

Training using other optimization methods

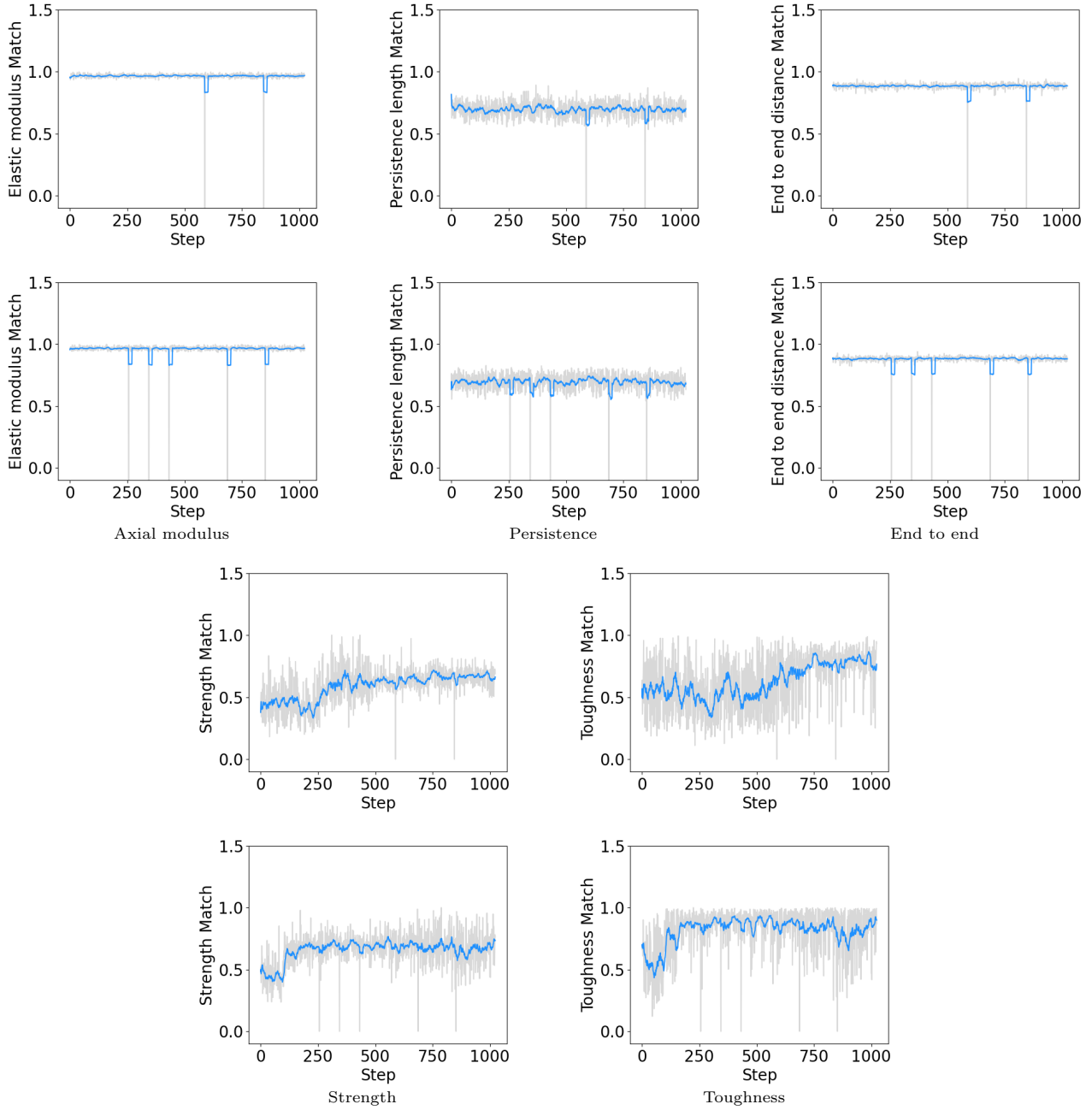


Figure S18: Component match degrees of reward function in the first (upper) and last (lower) training loop without thresholds. Average match degrees were obviously higher than the counterpart with thresholds. When focusing on best match degrees, these data did not outperform, which emphasized the robustness of convergence.

As introduced in the paper, the training for RL was not continuous: Training was finished by evolution of training loops: later training loop loaded the saved state of previous training loops and still had limited explorations. Due to the continuous optimization process of these methods (similar to single training loop), the first 1024 steps were compared.

As shown by the figures, TPE could not find a coefficient set of high reward value after 1024 step training. The real advantage of RL was further presented by the divergence of coefficients training with thresholds. The average and standard error of 20 best coefficient sets were compared in the Figure S19. For the coefficients, no significant differences were observed between RL and CMAES; For the standard error, all from the coefficients of RL were larger than CMAES. As we emphasized in the paper, the key feature is the balance of reward and stochasticity, and we have to do manual performance tests to compensate the insufficient sampling during training. Thus, a limited stochasticity was necessary for local minima prevention and the coefficient exploration when sampling was insufficient.

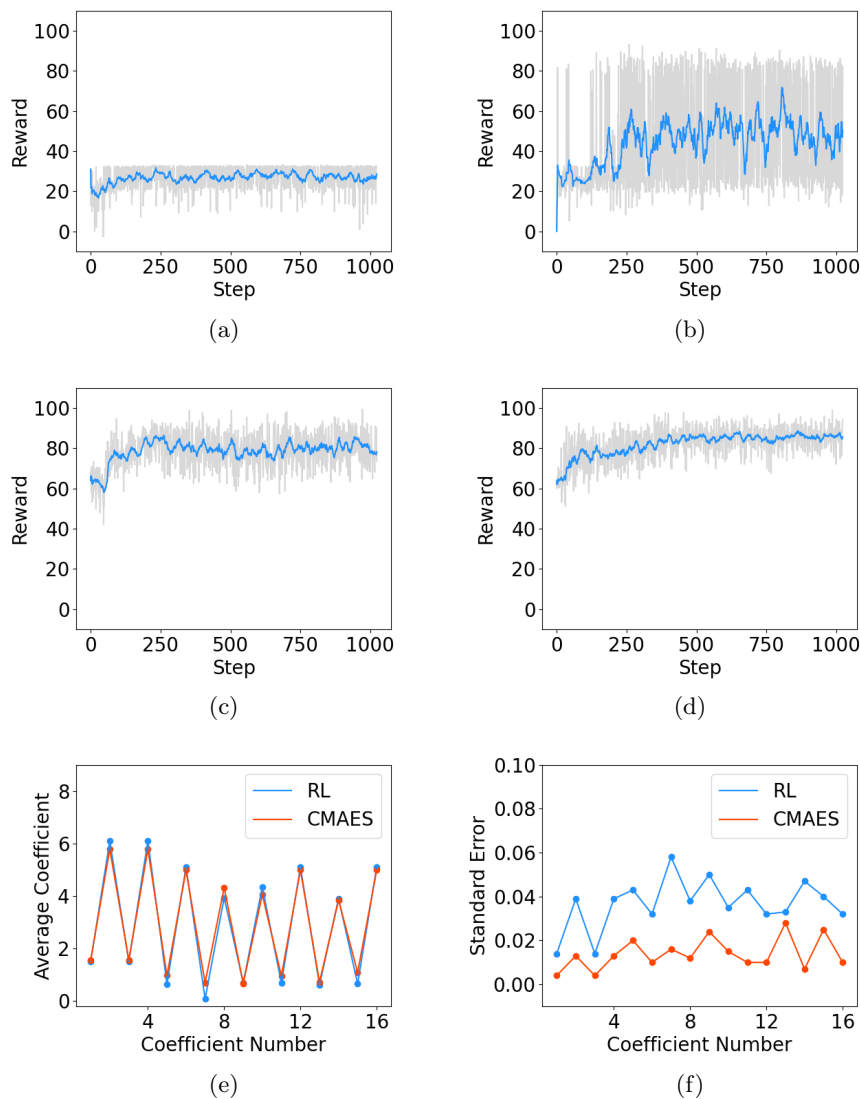


Figure S19: Training convergence and statistics from TPE and CMAES. (a) Training reward with step curve for TPE and (b) CMAES with thresholds. TPE did not find good coefficients with thresholds enabled. (c) Training reward with step curve for TPE and (d) CMAES without thresholds. (e) Average coefficient and (f) standard error for best 20 coefficient sets from RL and CMAES with thresholds. TPE and CMAES were chose to further validate the effectiveness of RL for potential parameterization. Owing to the continuous training of them and the training loop of RL, only the first 1024 steps were compared. When using thresholds, TPE could not hit high reward values, which stressed the capability of RL to deal with strong nonlinear problems. The critical comparison was the best coefficients from CMAES and RL with thresholds. The deviations of coefficients from RL was significantly higher than those from CMAES. As emphasized in the paper, transverse strength and toughness was only sampled once during training which required post-training manual performance check. Thus deviations from RL were critical to compensate the insufficient sampling to find a set of good coefficients.

Secondary summits of the bonded geometry parameter distributions

The harmonic potentials were appropriate for symmetric bonded geometry parameter distributions. However, secondary plateaus or summits were observed in the bonded geometry parameter distributions of CL2 beads (Figure S20). This phenomenon was caused by the rotational degrees of freedom of the hydroxyls and was more evident in the single-chain simulations, in which the branch beads were not restrained by HBonds. Ignoring the hydroxyl rotation is simple, but may cause problems in other cases.

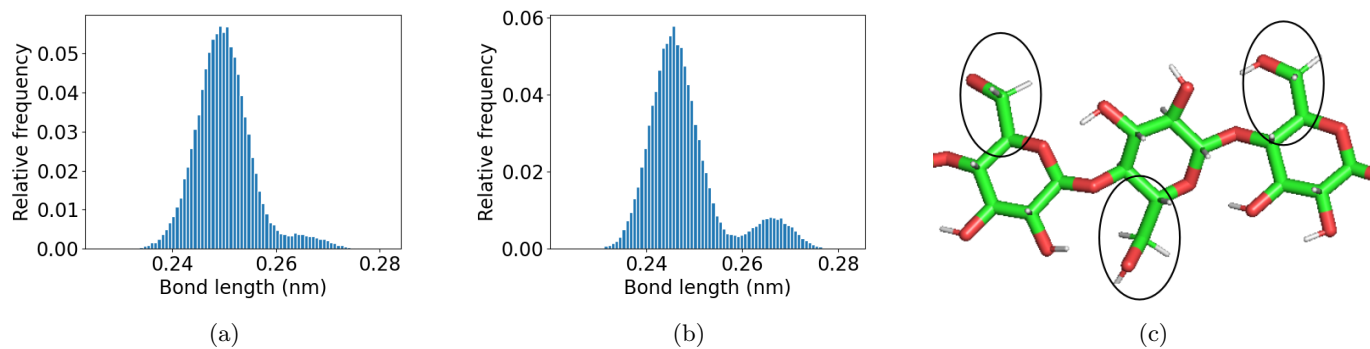


Figure S20: Secondary summits of the bonded geometry parameter distributions. (a) Bond length distributions of CL1-CL2 from mapped crystal trajectories and (b) single-chain trajectories. (c) The secondary plateaus of the bonded geometry parameters were caused by the rotational degrees of freedom of the branched hydroxyls, particularly in the single-chain simulations. Branched hydroxyls were packed into CL2 beads. This implies that the CG model cannot represent a specific rotational movement, that may be critical in certain situations.